

# The distribution, kinematics and luminosities of extreme helium stars as probes of their origin and evolution

A. Philip Monai<sup>1,2\*</sup>, P. Martin<sup>1,3</sup>, C. S. Jeffery<sup>1</sup>

<sup>1</sup>Armagh Observatory and Planetarium, College Hill, Armagh, BT61 9DG, UK

<sup>2</sup>School of Mathematics and Physics, Queen's University Belfast, Belfast, BT7 1NN, UK

<sup>3</sup>School of Physics, Trinity College Dublin, College Green, Dublin 2, Ireland

Last updated 2023 December 1 ; in original form 2023 September 29

## ABSTRACT

Hydrogen deficient stars include the cool R CrB variable (RCBs) and hydrogen-deficient carbon (HdCs) giants through extreme helium stars (EHes) to the very hot helium-rich subdwarfs (He-sdO and O(He) stars) and white dwarfs. With surfaces rich in helium, nitrogen and carbon, their origins have been identified with the merger of two white dwarfs. Using *Gaia* to focus on the EHes, we aim to identify progenitor populations and test the evolution models. *Gaia* DR3 measurements and ground-based radial velocities have been used to compute Galactic orbits using `galpy`. Each orbit has been classified by population; EHe stars are found in all of the thin disk, thick disk, halo and bulge, as are RCB, HdC and He-sdO stars. Spectral energy distributions were constructed for all EHes, to provide angular diameters, and hence radii and luminosities. The EHes fall into two luminosity groups divided at  $L \approx 2500 L_{\odot}$ . This supports theory for the origin of EHes, and is the strongest confirmation so far in terms of luminosity. The lower luminosity EHes correspond well with the post-merger evolution of a double helium white dwarf binary. Likewise, the higher luminosity EHes match the post-merger evolution of a carbon/oxygen plus helium white dwarf binary. In terms of parent populations, current models predict that double white dwarf mergers should occur in all Galactic populations, but favour mergers arising from recent star formation (i.e. thin disk), whereas the statistics favour an older epoch (i.e. thick disk).

**Key words:** parallaxes – proper motions – stars: AGB and post-AGB – stars: chemically peculiar – stars: fundamental parameters – stars: kinematics and dynamics

## 1 INTRODUCTION

Extreme helium stars (EHes) are low-mass stars of spectral types A and B (Jeffery 1996). Their low surface gravities indicate high luminosity-to-mass ratios. Helium dominates the surface composition, with hydrogen contributing less than one part per thousand (ppt, by number) and carbon between 3 and 30 ppt. Nitrogen, oxygen and other products of nucleosynthesis are also enhanced (Jeffery et al. 2011). Their radial-velocities and Galactic distribution suggest an origin in the Galactic bulge (Jeffery et al. 1987). R CrB (RCB) and O(He) stars have similar surface chemistries and luminosities but lower and higher surface temperatures respectively (Clayton 1996; Reindl et al. 2014). The RCB stars represent the most active members of a larger class of cool hydrogen-deficient carbon-rich giants (HdC stars) (Crawford et al. 2023). The surface properties of these three groups are best explained by evolution following the merger of a helium white dwarf with a carbon-oxygen white dwarf (Webbink 1984; Saio & Jeffery 2002), with their ultimate fate to become a hot hydrogen-deficient white dwarf. Naively speaking, an origin in the (old) Galactic bulge should be entirely consistent with the long delay time associated with the orbital decay of a double white dwarf binary via gravitational wave radiation.

Several EHes have higher surface gravities than the majority and are better understood in terms of evolution following the merger of two helium white dwarfs (Saio & Jeffery 2000). Such stars will evolve toward the helium main-sequence where they are observed as helium-rich sdO stars (He-sdOs) (Zhang & Jeffery 2012a) associated with the Galactic thick disk (Martin & Jeffery 2017), and considered younger than the Galactic bulge.

Binary-star population synthesis (BSPS) calculations suggest other pictures. Zhang et al. (2014) find that double helium white dwarf mergers should come predominantly from star formation more than 4 Gyr ago and carbon-oxygen + helium white dwarfs come from star formation between 0.5 and 2 Gyr ago. Yu & Jeffery (2010, 2011) find that the majority of mergers in the present epoch should arise from star formation more than 4 Gyr ago. Since actual orbital decay times depend on the white dwarf masses and initial separations, a sufficiently large sample of binaries from a given star-formation epoch that evolve to become double white dwarfs will continue to produce short-lived exotic stars long after their pre-white dwarf evolution is complete. Hence - studies of a present day sample of such stars must in fact derive from a long period of Galactic star formation and reflect a substantial range of actual ages.

Our main question (1) concerns the progenitor population(s) of EHes; that is, what are their distributions in position and age? Secondary questions concern (2) the relationship between EHe stars,

\* email: asish.philip.monai@armagh.ac.uk

HdC and RCB stars, O(He) stars and He-sdOs, and (3) the validity of the evolution models in terms of EHe masses and luminosities. Owing to their considerable heliocentric distances (1 – 8 kpc), reliable answers to (1) have only become accessible since the 3rd release of data from the *Gaia* project (Gaia Collaboration et al. 2016, 2023). In addition, answers to (2) and (3) require additional data for effective temperatures over a wide range of spectral types.

This paper combines the *Gaia* positional and proper motion data and ground-based radial velocity data (§ 2) to obtain full 6-space positions (§,3) and population classifications (§ 4). These data are supplemented with published photometry to build complete spectral energy distributions and hence angular radii and luminosities (§ 5). Masses are inferred from the measured surface gravities, where these are available. We present this analysis in detail for the EHeS. We have also carried out this analysis for comparison samples of related objects including RCB, and helium-rich subdwarfs. Since similar analyses have been carried out in part or in whole elsewhere (Geier 2020; Culpan et al. 2022; Tisserand et al. 2022, etc.), they are only discussed here in summary form.

## 2 OBSERVATIONS

The complete dataset for analysis contains the full 6-space position for every known member of the different classes of hydrogen-deficient stars together with spectroscopic and photometric measurements of effective temperature, surface gravity and interstellar extinction. The EHe sample was based on compilations by Jeffery et al. (1996); Clayton (1996) and Martin (2019).<sup>1</sup> In addition, we have included new EHeS discovered as part of the SALT survey of chemically peculiar subdwarfs (Jeffery et al. 2021). The primary criteria for inclusion are that each star should be included in *Gaia* Data Release 3 (DR3) and should have a known radial velocity.

The majority of EHe radial velocities come from Jeffery et al. (1987) and Jeffery et al. (2021). The former found no significant variability amongst all EHeS surveyed. With no evidence that any are binaries, Jeffery et al. (1987) argued that all must have been binaries at some time in the past. Where repeat observations have been obtained, none of the stars classified by Jeffery et al. (2021) and identified here as EHeS have yet been found to be binaries. A number are known to pulsate with irregular small-amplitude radial-velocity variations (Walker & Hill 1985; Lawson et al. 1993; Jeffery et al. 2001a), for which we adopt the mean velocity, or with regular large-amplitude radial-velocity variations (Lynas-Gray et al. 1984; Kilkenny et al. 1999), for which the system velocity is known precisely. We take the space velocities to be secure to within the errors shown. For the EHeS, the typical error is  $\sim \pm 3 \text{ km s}^{-1}$  and for the secondary sample, the typical error is  $\sim \pm 17 \text{ km s}^{-1}$ .

For the EHe sample, an additional criterion was the availability of measurements for effective temperatures ( $T_{\text{eff}}$ ) and surface gravities ( $\log g$ ). These measurements along with the extinction coefficients ( $E_{(B-V)}$ ) are presented in section 5. Table 1 shows the *Gaia* data (position, proper motion and parallax) and the radial velocity for the 27 stars in the EHe sample.

We studied the kinematics and the Galactic orbits of these stars and derived the angular diameters and luminosities from their spectral energy distributions. To compare this sample with the other

<sup>1</sup> DY Cen has been excluded from the EHe sample on the basis of its high hydrogen content and very rapid evolution (Jeffery et al. 2020). HD 144941 has been excluded as possibly the most extreme member of the magnetic massive helium-strong stars (Przybilla et al. 2021).

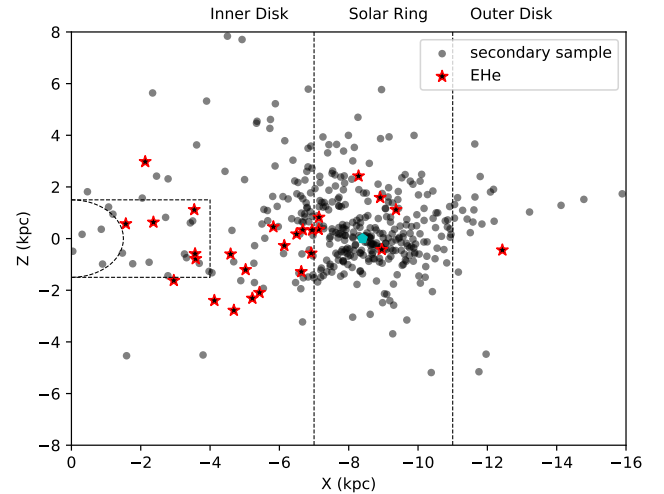


**Figure 1.** Distribution of sample in the Galactic  $X - Z$  plane. The red stars denote the primary sample and the grey dots denote the secondary sample. The position of the Sun is denoted by a filled cyan pentagon. The dashed ellipse shows the estimates of the inner bulge ( $R \sim 1.5$  kpc) and the dashed rectangle shows the estimates of the bar ( $X = \pm 4$  kpc,  $Y = \pm 1.5$  kpc,  $Z = \pm 1.5$  kpc) (Bland-Hawthorn & Gerhard 2016).

groups mentioned above, we compiled a secondary sample containing HdC, RCB, He-sdO, He-sdOB, and He-sdB stars based on Clayton (2012); Reindl et al. (2014); Geier (2020); Tisserand et al. (2020); Culpan et al. (2022); Tisserand et al. (2022) and Crawford et al. (2023). A list of these stars is provided in Appendix A.

## 3 ANALYSIS

### 3.1 Distances

*Gaia* DR3 parallaxes have been used to obtain distances. The zero points of the parallax measurements have been corrected as described by Lindegren et al. (2021) and the corrected parallax is given in Table 1.

Inverting a parallax to give a distance is only appropriate when measurement errors are negligible. As parallax measurements always contain significant errors, determining distance from parallax becomes an inference problem. Small absolute errors can translate into large errors in distance (Bailer-Jones 2015; Luri et al. 2018; Bailer-Jones et al. 2021). Once the fractional parallax error  $\sigma/\pi \geq 0.2$ , a simple inversion becomes noisy and gives an incorrect error estimate. This can be mitigated by the use of a properly normalised prior. Here an Exponentially Decreasing Space Density Prior is adopted, with one free parameter, the length scale, fixed at 1.35 kpc (Luri et al. 2018). Even though a Bayesian approach can give distance estimates from even a negative parallax measurement, the prior will always dominate when the fractional error in parallax is high. Three stars in the primary sample have fractional parallax error  $\sigma/\pi \geq 0.2$ : EC 20111–6902 (0.42), GALEX J184559.8–413827 (0.22) and V2205 Oph (0.21). We note that although these errors are significant, they are substantially improved over *Gaia* DR2. In particular, V2205 Oph had  $\sigma/\pi \geq 0.5$  in *Gaia* DR2.

Distance measurements obtained for the stars in the primary sample are reported in Table 1, where the errors correspond to the 68.27% confidence intervals.

**Table 1.** Astrometric data for EHe stars from *Gaia* including radial velocities, corrected parallax and the computed distance sorted by right ascension.

Star	$\alpha$	$\delta$	$\mu_\alpha$	$\mu_\delta$	$v$	$\pi$	Distance
	deg	deg	mas yr <sup>-1</sup>	mas yr <sup>-1</sup>	km s <sup>-1</sup>	mas	kpc
BD +37 442	29.64	38.57	-10.49±0.06	-7.27±0.07	-99.4±25.0 <sup>1</sup>	0.97±0.06	1.04 <sup>+0.06</sup> <sub>-0.07</sub>
LSS 99	103.69	-10.81	0.09±0.01	-0.59±0.01	109.0±3.0 <sup>2</sup>	0.17±0.01	5.73 <sup>+0.38</sup> <sub>-0.44</sub>
BD +37 1977	141.11	36.71	10.86±0.05	-11.77±0.05	-80.9±9.9 <sup>1</sup>	0.64±0.07	1.60 <sup>+0.16</sup> <sub>-0.20</sub>
BD +10 2179	159.73	10.06	-10.37±0.06	-4.86±0.04	155.2±2.8 <sup>2</sup>	0.52±0.05	1.99 <sup>+0.19</sup> <sub>-0.24</sub>
BX Cir	210.40	-66.17	-8.34±0.01	2.22±0.02	-83.0±2.0 <sup>3</sup>	0.31±0.02	3.29 <sup>+0.21</sup> <sub>-0.23</sub>
HD 124448	213.74	-46.29	-6.54±0.04	-0.05±0.03	-65.0±3.0 <sup>2</sup>	0.65±0.03	1.56 <sup>+0.07</sup> <sub>-0.08</sub>
PG 1415+492	214.26	48.96	1.1±0.03	-6.55±0.03	54.0±1.0 <sup>4</sup>	0.37±0.03	2.76 <sup>+0.21</sup> <sub>-0.25</sub>
CoD -48 10153	234.75	-48.60	-6.07±0.02	-6.4±0.02	-4.5±2.5 <sup>2</sup>	0.14±0.02	6.88 <sup>+0.81</sup> <sub>-1.03</sub>
V2205 Oph	247.15	-9.33	-2.27±0.03	3.06±0.02	-69.3±1.0 <sup>2</sup>	0.14±0.03	6.85 <sup>+0.95</sup> <sub>-1.26</sub>
V652 Her	252.02	13.26	-4.24±0.04	3.76±0.03	2.0±0.5 <sup>5</sup>	0.66±0.05	1.55 <sup>+0.11</sup> <sub>-0.13</sub>
V2076 Oph	265.46	-17.90	-6.25±0.03	2.56±0.02	76.8±2.6 <sup>2</sup>	0.56±0.03	1.79 <sup>+0.09</sup> <sub>-0.10</sub>
CoD -46 11775	265.64	-46.98	-3.79±0.03	-0.95±0.02	-90.7±9.3 <sup>2</sup>	0.21±0.03	4.91 <sup>+0.62</sup> <sub>-0.81</sub>
LSS 4357	266.11	-19.63	-3.51±0.02	1.55±0.01	-99.0±10.0 <sup>2</sup>	0.15±0.02	6.77 <sup>+0.70</sup> <sub>-0.87</sub>
V2244 Oph	267.86	-1.72	-0.13±0.02	-8.34±0.01	-8.3±2.9 <sup>6</sup>	0.19±0.02	5.29 <sup>+0.43</sup> <sub>-0.51</sub>
NO Ser	270.98	-1.01	0.3±0.02	-2.02±0.02	-21.1±4.6 <sup>2</sup>	0.37±0.02	2.75 <sup>+0.12</sup> <sub>-0.13</sub>
LS IV+6 2	271.73	6.37	-3.01±0.03	-8.84±0.03	-24.0±4.0 <sup>2</sup>	0.63±0.03	1.61 <sup>+0.07</sup> <sub>-0.08</sub>
PV Tel	275.81	-56.63	-1.24±0.02	-7.81±0.02	-170.9±2.3 <sup>2</sup>	0.27±0.02	3.67 <sup>+0.27</sup> <sub>-0.32</sub>
LSS 5121	280.82	-18.52	-2.0±0.02	0.52±0.02	-62.0±6.0 <sup>2</sup>	0.21±0.02	4.89 <sup>+0.38</sup> <sub>-0.45</sub>
GALEX J184559.8-413827	281.50	-41.64	0.24±0.04	0.1±0.03	-57.6±6.1 <sup>7</sup>	0.18±0.04	5.56 <sup>+0.90</sup> <sub>-1.27</sub>
LS IV -14 109	284.91	-14.44	-0.36±0.02	-0.43±0.02	-7.3±2.7 <sup>8</sup>	0.25±0.02	3.96 <sup>+0.29</sup> <sub>-0.34</sub>
GALEX J191049.5-441713	287.71	-44.29	-2.7±0.05	-2.93±0.04	1.0±3.0 <sup>9</sup>	0.70±0.05	1.45 <sup>+0.09</sup> <sub>-0.11</sub>
V1920 Cyg	296.32	33.97	0.11±0.02	-6.24±0.02	-89.9±1.9 <sup>2</sup>	0.23±0.02	4.39 <sup>+0.29</sup> <sub>-0.33</sub>
EC 19529-4430	299.13	-44.37	-6.8±0.03	-13.22±0.03	5.0±3.0 <sup>9</sup>	0.21±0.04	4.77 <sup>+0.71</sup> <sub>-0.98</sub>
EC 20111-6902	304.04	-68.89	2.65±0.06	-1.72±0.08	-81.0±3.0 <sup>9</sup>	0.19±0.08	5.08 <sup>+1.27</sup> <sub>-1.96</sub>
EC 20236-5703	306.90	-56.90	1.94±0.04	-13.34±0.04	-74.0±3.0 <sup>9</sup>	0.26±0.04	3.94 <sup>+0.50</sup> <sub>-0.67</sub>
BPS CS 22940-0009	307.58	-59.84	2.53±0.03	-10.79±0.03	32.7±2.0 <sup>4</sup>	0.47±0.03	2.16 <sup>+0.15</sup> <sub>-0.17</sub>
FQ Aqr	312.84	2.31	-0.62±0.02	-6.18±0.02	23.7±1.4 <sup>6</sup>	0.21±0.02	4.84 <sup>+0.39</sup> <sub>-0.46</sub>

1.de Bruijne & Eilers (2012), 2.Jeffery et al. (1987), 3.Kilkenny et al. (1999), 4.Martin et al. (2017), 5.Jeffery et al. (2015), 6.Jeffery et al. (2001a), 7.Kawka et al. (2015), 8.Lawson et al. (1993), 9.Jeffery et al. (2021)

### 3.2 Galactic and orbital parameters

Figure 1 shows the positions of the stars projected onto the Galactic  $X-Z$  plane, where  $Z$  is the distance from the Galactic plane, and  $X$  from the Galactic Centre (GC). We define the inner disk  $R < 7$  kpc, the Solar ring  $7 < R < 11$  kpc and the outer disk  $R > 11$  kpc from the GC (Bland-Hawthorn & Gerhard 2016). Estimates of the extent of the bulge and/or bar are also shown. Most of the stars in our sample lie between the Sun and the GC. Seven EHe stars are situated within or close to the bulge or bar. This highlights the capabilities of *Gaia* in separating out sources that are close to the Galactic bulge. This figure also highlights that our sample is subject to Malmquist bias, or the preferential detection at large distances of intrinsically brighter objects. The question this observation raises is whether this constraint causes any bias in our understanding of group kinematics and further inferences.

Using the observed values of right ascension ( $\alpha$ ), declination ( $\delta$ ), distance, proper motion ( $\mu_\alpha$  and  $\mu_\delta$ ) and radial velocity ( $v$ ), the Galactic velocity components were calculated following the method outlined in Randall et al. (2015). The left-handed system for the velocity components is used here, where  $U$  is the Galactic radial velocity, positive towards the Galactic Centre,  $V$  is the Galactic rotational velocity in the direction of the Galactic rotation and  $W$  is the component positive towards the North Galactic Pole. This calculation assumes the distance of the Sun from the Galactic Centre to be  $8.25 \pm 0.33$  kpc (GRAVITY Collaboration

et al. 2021), its motion relative to the LSR to have components  $(v_x, v_y, v_z) = (9.5, 17.3, 8.56)$  km s<sup>-1</sup> and the velocity of the LSR to be  $V_{\text{LSR}} = 233.4 \pm 1.5$  km s<sup>-1</sup> (Drimmel & Poggio 2018; Reid & Brunthaler 2020; GRAVITY Collaboration et al. 2021).

Orbits for individual stars (Fig. 2) have been calculated using `galpy`<sup>2</sup>, a python package for Galactic-dynamic calculations (Bovy 2015). The orbits were computed using the potential MWPotential 2014; this model is fit to dynamical data of the Milky Way. Although this is not the best possible current model, it was chosen as it gives a realistic model of the Milky Way's gravitational potential that is simple and easy to use. It consists of a bulge modelled as a power-law density profile that is exponentially cut off with a power-law exponent of  $-1.8$  and a cut-off radius of 1.9 kpc, a Miyamoto-Nagai Potential disc (Miyamoto & Nagai 1975) and a dark-matter halo described by a Navarro-Frenk-White potential (Navarro et al. 1996). These orbits when integrated over 3 Gyrs give values for the maximum distance from the GC (apocentre  $R_a$ ), minimum distance to the GC (pericentre  $R_p$ ), maximum vertical amplitude ( $Z_{\text{max}}$ ) and the z-component of the angular momentum ( $J_z$ ). The quantities  $R_a$  and  $R_p$  are obtained over a revolution of  $2\pi$  radians, measured on the Galactic plane. From these distances, the orbital eccentricity can

<sup>2</sup> <http://github.com/jobovy/galpy>

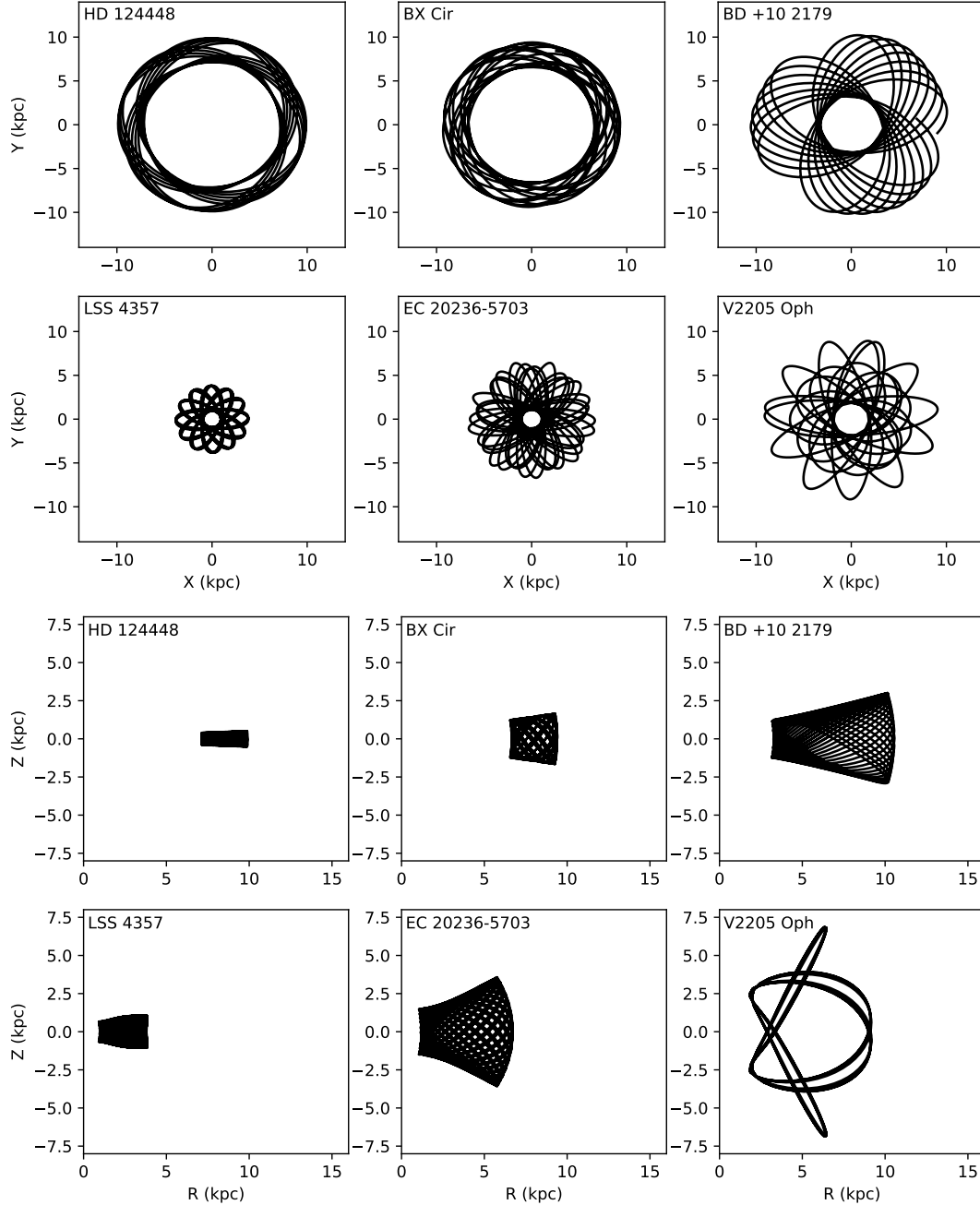


**Figure 2.** *galpy* orbits for 6 representative EHe stars computed for 3 Gyrs from their current positions. The top panels show motion in the X – Y plane, the bottom panels show motion in the R – Z plane, with the Galactic centre being at the origin. The panels illustrate thin-disk (HD 124448), thick disk (BX Cir), halo (BD +10 2179), bulge (LSS 4357), halo (EC 20236–5703), and halo (V2205 Oph) orbits.

be computed as

$$e = \frac{R_a - R_p}{R_a + R_p}. \quad (1)$$

Using *galpy*, 100 orbits were computed for each star, with starting values distributed randomly over the range of errors associated with each one so as to obtain a sample of likely orbits. From this sample, the orbit with the highest likelihood (mode) was selected with the rest being used to compute the statistical errors (standard deviation) on the orbital elements. These quantities are shown in Table 2, along with the stars’ Galactic velocities.

### 3.3 Colour-magnitude diagram

When combined with the extinction coefficient ( $E_{B-V}$ ), *Gaia* distances and colours provide us with absolute magnitudes  $M_V$ . These can be defined in terms of the apparent *Gaia* magnitude  $G$  and colours  $G_{BP} - G_{RP}$  using the Johnson-Cousins relation from [Riello et al. \(2021\)](#):

$$V = G + 0.02704 - 0.01424(G_{BP} - G_{RP}) + 0.2156(G_{BP} - G_{RP})^2 - 0.01426(G_{BP} - G_{RP})^3, \quad (2)$$

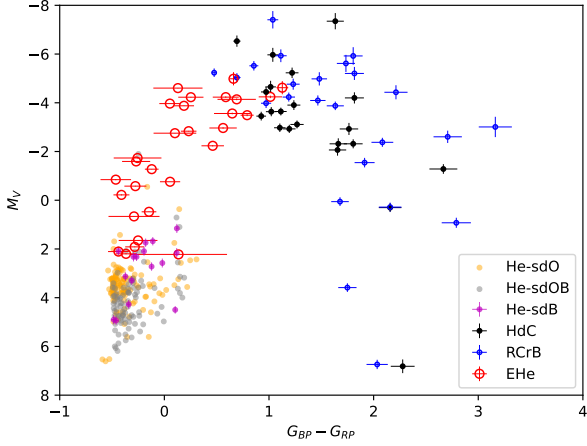


**Figure 3.** Colour magnitude diagram of the whole sample obtained from the *Gaia* magnitude and colours as given in S. 3.3.

$$M_V = V - 5(\log_{10} d - 1) - 3.1E_{B-V}, \quad (3)$$

where  $V$  is the apparent visual magnitude and  $d$  is the distance in parsecs.

Since Eqn (2) has been derived for stars with hydrogen-rich atmospheres, we compared the transformed V magnitude with V magnitudes from SIMBAD. The latter are, on average,  $\approx 0.02$  mag larger for  $G_{BP} - G_{RP} > 0$  decreasing to  $\approx 0.05$  mag smaller for  $G_{BP} - G_{RP} \approx -0.4$ , with a mean scatter of  $\approx \pm 0.02$  mag ( $1\sigma$ ). The small trend is consistent with a reduced contribution of the Balmer series to the EHe star colours. The transformed EHe V magnitudes may be improved by applying the correction

$$\delta = 0.00759 + 0.11452(G_{BP} - G_{RP}) - 0.11589(G_{BP} - G_{RP})^2. \quad (4)$$

The colour-magnitude diagram of the whole sample plotted from the *Gaia* colours<sup>3</sup> is shown in Fig. 3. This shows a progression from the cool HdC stars and RCB stars to the hotter EHe and He-SdO stars. There is an overlap between the coolest EHe stars and the hottest HdCs.

## 4 KINEMATICS

With information about Galactic 3D space velocities and orbits, an attempt may be made to connect both classes and individual stars with parent populations. In the following we describe our classification scheme, and then discuss the classifications in terms of spatial and kinematical distributions.

### 4.1 Classification.

The population classification described in [Martin et al. \(2017\)](#) has been augmented with a classification for the bulge. We define the extent of the bulge based on estimates for the bulge and bar from [Bland-Hawthorn & Gerhard \(2016\)](#) who state that it is difficult to

<sup>3</sup> Author's note in proof: Fig. 3 is based on mean *Gaia* magnitudes. For RCB and HdC stars observed during a decline, mean *Gaia* magnitudes do not reflect the luminosity at maximum light and here applies to RCB and HdC stars with  $M_V > -3$ .

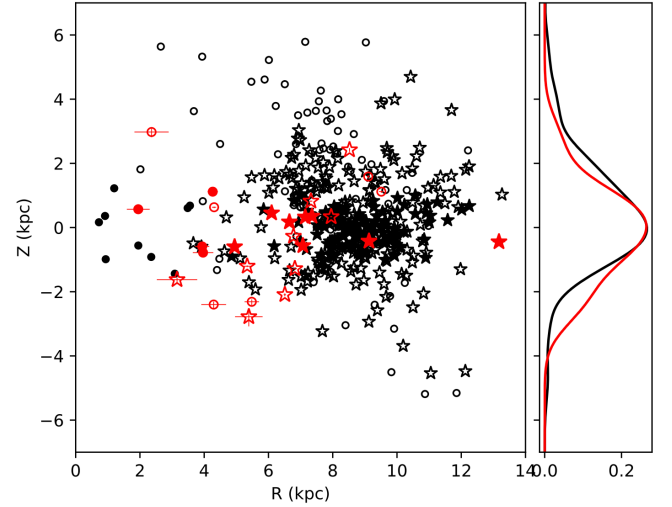


**Figure 4.** Distribution of the sample in the Z plane plotted as a function of the galactocentric distance. Red symbols indicate the primary sample of EHe stars and the black symbols denote the secondary sample. The sample has been classified into the disc and spherical components as given in section 4. The circles represent the spherical components with the filled circles denoting the bulge and the open circles denoting the halo stars. The stars represent the disk components with the filled stars denoting the thin disk and the open circles denoting the thick disk stars.

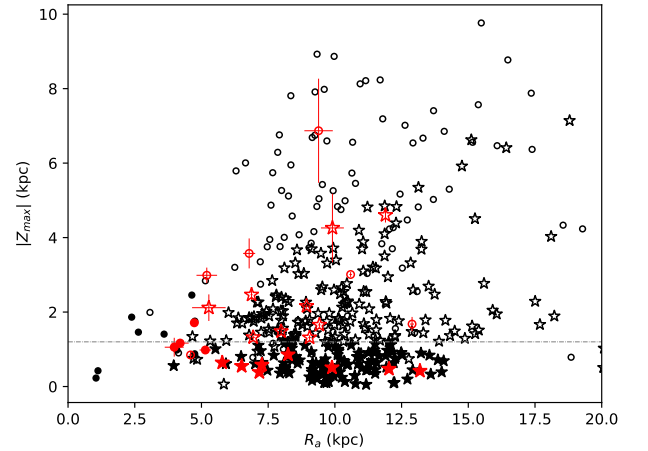


**Figure 5.** The maximum distance in the Z direction ( $Z_{\max}$ ) is plotted as a function of the maximum distance of the star from the Galactic center ( $R_a$ ). The symbols have the same meaning as defined in Fig. 4. The dashed line represents the thin disk cut-off height of 1.2 kpc set to distinguish between the thick and thin disk.

separate the outer bulge from the bar; we therefore do not distinguish the bar from the bulge.

Broadly:

(i) Stars with low eccentricity and low inclination orbits are identified with the Galactic disk. These are further subdivided into

**Thin Disk (TH):** stars with  $Z_{\max} < 1.2$  kpc and falling within the thin disk regime in the Toomre diagram.

**Thick Disk (TK):** stars with  $Z_{\max} > 1.2$  kpc and falling



**Table 2.** Orbital parameters and Galactic velocities of Extreme Helium stars sorted as in Table 1. The last column shows the population classification where TH = thin disk, TK = thick disk, H = halo and B = bulge.  $f = p(\text{thick})/p(\text{thin})$  shows the likelihood of a star belonging to the thick or thin disk. The stars for which the orbits were classified by inspection have been marked with a \*.

Star	$U$ km s <sup>-1</sup>	$V$ km s <sup>-1</sup>	$W$ km s <sup>-1</sup>	$J_z$ kpc km s <sup>-1</sup>	$e$	$R_a$ kpc	$R_p$ kpc	$Z_{\max}$ kpc	$\log(f)$	pop
BD +37 442	-98.1 <sup>+10.5</sup> <sub>-10.6</sub>	210.1 <sup>+8.5</sup> <sub>-8.4</sub>	0.9 <sup>+5.7</sup> <sub>-5.6</sub>	1971.9±75.3	0.33±0.04	12.03±0.19	6.05±0.44	0.47±0.03	-0.82	TH
LSS 99	10.0 <sup>+1.6</sup> <sub>-1.8</sub>	175.3 <sup>+0.8</sup> <sub>-0.8</sub>	-5.0 <sup>+0.2</sup> <sub>-0.2</sub>	2352.5±31.3	0.25±0.00	13.19±0.20	7.86±0.13	0.42±0.02	-0.85	TH
BD +37 1977	-20.4 <sup>+4.3</sup> <sub>-4.5</sub>	114.4 <sup>+4.3</sup> <sub>-5.1</sub>	-20.8 <sup>+4.3</sup> <sub>-4.4</sub>	1646.3±44.1	0.48±0.02	12.89±0.28	4.52±0.18	1.68±0.20	-	H
BD +10 2179*	-79.6 <sup>+3.2</sup> <sub>-4.4</sub>	189.9 <sup>+0.7</sup> <sub>-0.7</sub>	110.2 <sup>+1.3</sup> <sub>-1.6</sub>	1161.0±26.1	0.53±0.02	10.59±0.15	3.26±0.17	3.01±0.06	-	H
BX Cir*	-130.2 <sup>+3.4</sup> <sub>-3.4</sub>	280.7 <sup>+2.1</sup> <sub>-1.8</sub>	114.7 <sup>+1.9</sup> <sub>-1.9</sub>	1827.1±20.3	0.17±0.01	9.42±0.14	6.65±0.03	1.66±0.06	0.91	TK
HD 124448	-34.9 <sup>+1.5</sup> <sub>-1.4</sub>	292.6 <sup>+1.2</sup> <sub>-1.2</sub>	22.0 <sup>+0.6</sup> <sub>-0.6</sub>	2003.4±16.7	0.16±0.01	9.89±0.17	7.14±0.03	0.51±0.01	-0.8	TH
PG 1415+492	-27.1 <sup>+0.6</sup> <sub>-0.8</sub>	230.3 <sup>+0.9</sup> <sub>-1.2</sub>	75.4 <sup>+0.7</sup> <sub>-0.7</sub>	2094.5±7.8	0.16±0.00	11.90±0.08	8.67±0.03	4.60±0.19	13.57	TK
CoD -48 10153	-140.9 <sup>+3.9</sup> <sub>-0.9</sub>	0.9 <sup>+11.8</sup> <sub>-15.9</sub>	7.5 <sup>+0.5</sup> <sub>-0.5</sub>	494.0±19.9	0.51±0.02	4.59±0.03	1.50±0.09	0.85±0.09	-	H
V2205 Oph	111.3 <sup>+20.1</sup> <sub>-10.8</sub>	299.7 <sup>+6.6</sup> <sub>-1.1</sub>	103.5 <sup>+5.2</sup> <sub>-6.9</sub>	563.8±172.2	0.57±0.07	9.39±0.53	2.59±0.36	6.87±1.47	-	H
V652 Her	4.8 <sup>+0.5</sup> <sub>-0.6</sub>	269.4 <sup>+0.3</sup> <sub>-0.5</sub>	50.4 <sup>+0.8</sup> <sub>-1.1</sub>	1847.5±12.8	0.14±0.01	9.05±0.02	6.87±0.08	1.31±0.06	0.21	TK
V2076 Oph	34.3 <sup>+1.6</sup> <sub>-1.5</sub>	251.8 <sup>+0.4</sup> <sub>-0.4</sub>	66.2 <sup>+1.0</sup> <sub>-1.1</sub>	1525.8±16.4	0.24±0.01	8.25±0.07	5.04±0.06	0.86±0.03	-0.47	TH
CoD -46 11775	-58.2 <sup>+8.6</sup> <sub>-9.6</sub>	235.2 <sup>+5.0</sup> <sub>-4.2</sub>	98.8 <sup>+2.7</sup> <sub>-4.0</sub>	910.6±98.3	0.02±0.02	4.20±0.36	4.00±0.34	1.17±0.06	-	B
LSS 4357	135.1 <sup>+18.4</sup> <sub>-14.9</sub>	234.4 <sup>+13.3</sup> <sub>-6.0</sub>	142.6 <sup>+4.3</sup> <sub>-5.6</sub>	297.6±115.8	0.61±0.10	3.98±0.22	0.98±0.35	1.06±0.27	-	B
V2244 Oph	-39.3 <sup>+1.2</sup> <sub>-1.4</sub>	128.4 <sup>+1.6</sup> <sub>-2.2</sub>	-85.8 <sup>+2.2</sup> <sub>-2.7</sub>	545.7±31.7	0.40±0.03	4.73±0.05	2.04±0.13	1.71±0.08	-	B
NO Ser	45.6 <sup>+2.3</sup> <sub>-2.3</sub>	217.2 <sup>+1.8</sup> <sub>-1.7</sub>	-11.3 <sup>+0.6</sup> <sub>-0.6</sub>	1362.2±19.7	0.15±0.01	6.51±0.05	4.85±0.10	0.55±0.02	-0.77	TH
LS IV+6 2	-25.5 <sup>+1.7</sup> <sub>-1.8</sub>	195.1 <sup>+1.5</sup> <sub>-1.5</sub>	-1.6 <sup>+0.5</sup> <sub>-0.5</sub>	1331.3±20.5	0.25±0.01	7.17±0.03	4.29±0.10	0.38±0.01	-0.87	TH
PV Tel	135.9 <sup>+1.1</sup> <sub>-1.0</sub>	236.4 <sup>+1.2</sup> <sub>-1.4</sub>	38.0 <sup>+0.7</sup> <sub>-0.8</sub>	1256.8±40.2	0.40±0.00	8.94±0.27	3.84±0.09	2.16±0.04	2.23	TK
LSS 5121	93.5 <sup>+4.0</sup> <sub>-4.3</sub>	223.2 <sup>+2.3</sup> <sub>-2.1</sub>	68.6 <sup>+1.3</sup> <sub>-1.5</sub>	802.2±53.4	0.32±0.02	5.15±0.15	2.65±0.18	0.98±0.04	-	B
GALEX										
J184559.8-413827	1.9 <sup>+8.3</sup> <sub>-6.4</sub>	264.3 <sup>+1.2</sup> <sub>-1.1</sub>	19.7 <sup>+1.4</sup> <sub>-1.3</sub>	847.1±155.5	0.22±0.05	5.28±0.26	3.35±0.54	2.12±0.34	2.1	TK
LS IV -14 109	59.7 <sup>+2.2</sup> <sub>-2.7</sub>	233.6 <sup>+1.1</sup> <sub>-1.2</sub>	13.1 <sup>+0.3</sup> <sub>-0.3</sub>	1160.5±39.4	0.17±0.01	5.78±0.09	4.08±0.17	0.64±0.03	-0.69	TH
GALEX										
J191049.5-441713	-23.7 <sup>+1.6</sup> <sub>-1.6</sub>	228.7 <sup>+0.5</sup> <sub>-0.6</sub>	20.5 <sup>+0.7</sup> <sub>-0.7</sub>	1617.5±17.4	0.09±0.01	7.26±0.05	6.11±0.09	0.58±0.02	-0.74	TH
V1920 Cyg	-0.9 <sup>+0.5</sup> <sub>-0.6</sub>	155.2 <sup>+1.2</sup> <sub>-1.2</sub>	-64.6 <sup>+1.3</sup> <sub>-1.5</sub>	1271.5±15.0	0.33±0.01	7.99±0.03	4.01±0.09	1.48±0.10	0.53	TK
EC 19529-4430	-61.3 <sup>+1.5</sup> <sub>-2.2</sub>	-61.1 <sup>+13.0</sup> <sub>-18.2</sub>	98.3 <sup>+4.0</sup> <sub>-3.4</sub>	-314.5±117.4	0.64±0.15	5.20±0.29	1.13±0.55	2.99±0.22	-	H
EC 20111-6902	-40.8 <sup>+11.9</sup> <sub>-13.7</sub>	279.8 <sup>+3.4</sup> <sub>-2.1</sub>	8.0 <sup>+3.3</sup> <sub>-5.1</sub>	1523.0±138.9	0.26±0.02	9.91±0.14	5.86±0.29	4.26±0.92	11.47	TK
EC 20236-5703	127.7 <sup>+4.6</sup> <sub>-5.7</sub>	67.1 <sup>+6.0</sup> <sub>-9.1</sub>	36.2 <sup>+1.1</sup> <sub>-1.2</sub>	368.5±101.0	0.71±0.05	6.79±0.06	1.15±0.27	3.57±0.42	-	H
BPS CS										
22940-0009	-0.5 <sup>+1.2</sup> <sub>-1.3</sub>	142.4 <sup>+2.1</sup> <sub>-2.2</sub>	-20.5 <sup>+0.7</sup> <sub>-0.7</sub>	982.0±39.3	0.40±0.02	6.94±0.06	2.96±0.14	1.32±0.06	0.27	TK
FQ Aqr	-3.9 <sup>+0.4</sup> <sub>-0.4</sub>	198.7 <sup>+1.2</sup> <sub>-1.4</sub>	-56.3 <sup>+1.2</sup> <sub>-1.6</sub>	1290.5±22.3	0.13±0.01	6.88±0.01	5.28±0.08	2.47±0.14	3.2	TK

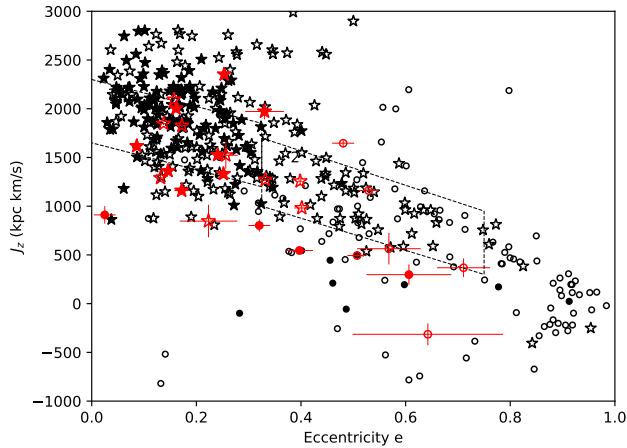


**Figure 6.** The  $z$  component of angular momentum plotted as a function of eccentricity. The symbols have the same meaning as defined in Fig. 4. The dashed regions indicate estimates for the thin and thick disk stars from Pauli et al. (2003).

within the thick disk regime in the Toomre diagram.

(ii) Stars with high eccentricity orbits and/or high orbital inclination are identified with spherical components. They are divided into:

**Bulge (B):** stars with low angular momentum, which come in close proximity to the Galactic Centre and stay in the inner disk, i.e.  $J_z < 1000$  kpc km s<sup>-1</sup>,  $|X| \leq 4$  kpc,  $|Y| \leq 1.5$  kpc and  $|Z| \leq 1.5$  kpc, or have  $R_a < 5$  kpc and  $e > 0.4$ .

**Halo (H):** stars with  $Z_{\max} > 1.2$  kpc and  $R_a > 7$  kpc or stars with high orbital inclination.

The classifications derived using the above criteria are shown in Table 2. A justification for these criteria will be given in the following subsection. The orbits for stars which clearly do not match any of the above categories were classified by inspection. A similar classification scheme was applied to the stars in the secondary sample.

## 4.2 Justification.

Figure 4 shows the  $Z$ -distribution of the sample members as a function of galactocentric distance  $R$ . The EHe sample appears to be centred on the disk with a Gaussian distribution along the  $Z$  axis,

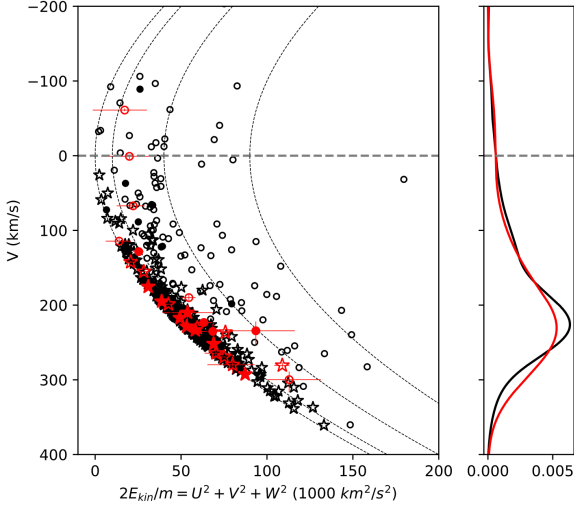


**Figure 7.** Galactic rotational velocity plotted against the total kinetic energy. The symbols have the same meaning as defined in Fig. 4. The parabolic curves denote line of equal velocity ( $V_{\perp} = (U^2 + W^2)^{1/2}$ ) at 0, 100, 300 and 400  $\text{km s}^{-1}$  respectively. The histogram with a bin size = 20  $\text{km s}^{-1}$  depicts the Galactic rotational velocities of the whole sample. The red and black bins refer to their respective samples. The grey dashed line represents  $V = 0$  with the stars above it showing retrograde motion and the stars below it showing prograde motion.

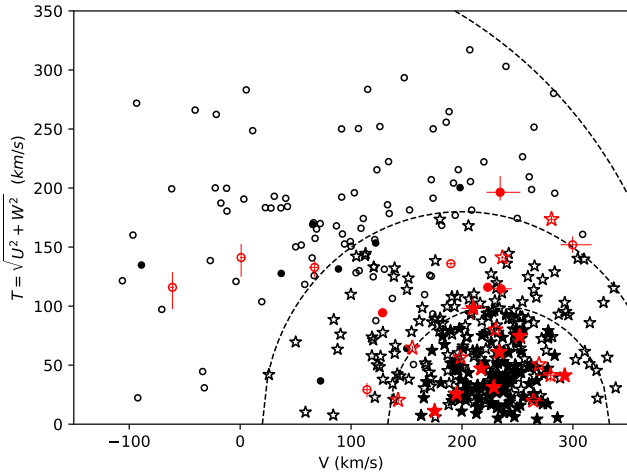


**Figure 8.** The Toomre diagram shows the kinematics of the sample. The symbols have the same meaning as defined in Fig. 4. The dotted lines correspond to predictions of Toomre diagrams from the Besançon Galactic models (Robin et al. 2003) for the thin disk ( $\leq 100 \text{ km s}^{-1}$ ), thick disk ( $\leq 180 \text{ km s}^{-1}$ ) and halo stars ( $\leq 400 \text{ km s}^{-1}$ ).

skewed slightly to negative  $Z$ . The  $Z$ -distribution of stars in all other classes is broadly similar, although skewed in the opposite sense. The scale height of both Gaussian distributions appears to exceed 2 kpc, so the samples as a whole (EHe and all others) cannot belong to the thin disk alone.

The thin and thick discs kinematically overlap one another in a way that makes it difficult to find a better selection criteria capable of distinguishing them. Boyy (2011) suggests that there may not be a separation between thin and thick discs implying that the transition

between them is a continuum. Our adopted definition for the thin disk extent,  $|Z_{\text{max}}| < 1.2 \text{ kpc}$ , is based on a relationship between the well-established scale heights of the thin disk and the thick disk (Ma et al. 2017),  $W$  values, and their number densities (Bensby et al. 2014).

We define

$$p(z) = n e^{-(z/h)^2} \quad (5)$$

as the probability of a star being found at height  $z$  in a population with a Gaussian distribution  $e^{-(z/h)^2}$ , where  $h$  is the scale height and  $n$  is the normalisation fraction of the population. Based on this relationship, we can obtain the likelihood that a star at  $Z_{\text{max}}$  belongs to either the thin disk or the thick disk, such that stars with  $|Z_{\text{max}}| = 1.2 \text{ kpc}$  have an equal likelihood ( $\sim 1$ ) of being either. The log likelihood of a star belonging to the thick disk rather than the thin disk,  $f = p(\text{thick})/p(\text{thin})$ , is shown in Table 2. Thus, the thin and thick disk assignments are  $> 70\%$  secure in all cases except V652 Her, V2076 Oph, and BPS CS 22940–0009, which all have a  $> 33\%$  chance of being mis-classified.

Figure 5 shows the apocentric positions of the sample members in terms of  $|Z_{\text{max}}|$  and  $R_a$ . This representation helps to separate classes because it combines the full orbital information with the spatial information. It clearly distinguishes the thin disk EHe stars from the thick disk and halo, but is not so good at separating out thick disk and halo stars, or thin disk and bulge stars. The same holds for stars in the secondary samples. There is a deficit of stars with high  $Z_{\text{max}}$  and low  $R_{\text{ap}}$ . This ‘zone of avoidance’ would correspond to stars in highly inclined orbits which are not expected to be numerous.

A method frequently used for population classification compares the  $Z$ -component of angular momentum ( $J_z$ ) with orbital eccentricity (Fig. 6) (cf. Pauli et al. 2003). Due to the low eccentricity of the disk stars, they tend to cluster around  $e \approx 0.2 \pm 0.1$  and  $J_z \approx 2000 \pm 500$ . This diagram was originally devised to identify thick disk stars in the local neighbourhood; because our sample volume is much larger than Pauli et al. (2003), some thick disk EHe stars lie outside Pauli’s region 2.

Figure 7 shows the kinetic energy  $2E_{\text{kin}}/m = U^2 + V^2 + W^2$  as a function of the rotational component  $V$ . Contours show the velocity perpendicular to Galactic rotation at certain values, where  $V_{\perp} = (U^2 + W^2)^{1/2}$ . Any value for which  $V_{\perp} > 100 \text{ km s}^{-1}$  implies a non-disk orbit. The higher the value of  $2E_{\text{kin}}/m$ , the more the orbit deviates from a circular orbit. This highlights stars which do not belong to the disk. We note a number of stars in retrograde motion, particularly the EHe star EC 19529–4430.

The Toomre diagram (Figure 8) has been used to classify the stars into their populations using their space velocities  $T \equiv V_{\perp} = (U^2 + W^2)^{1/2}$  versus  $V$ . Based on the predictions from the Besançon Galactic models (Robin et al. 2003), we identify stars within 100  $\text{km s}^{-1}$  of the solar motion to be likely thin disk stars, within 180  $\text{km s}^{-1}$  to be likely thick disk stars and those within 400  $\text{km s}^{-1}$  to be halo stars.

A useful tool in identifying halo stars with low eccentricities is the ‘normalized  $z$ -extent’, which can be substituted as a measure of the orbital inclination, given by

$$z_n = \frac{Z_{\text{max}}}{R(Z_{\text{max}})} \quad (6)$$

where  $R(Z_{\text{max}})$  is the galactocentric distance when the star is at  $Z_{\text{max}}$ .

As this paper was being completed, we received a preprint by Tisserand et al. (2023) presenting a similar analysis for HdC, RCB and EHe stars. Their sample of 16 EHe stars compares with our sample

**Table 3.** Population statistics for various classes of hydrogen-deficient star.

Category	N	Thin Disk	Thick Disk	Halo	Bulge
EHe	27	8	9	6	4
RCB	38	9	13	8	8
HdC	8	3	3	2	0
He-sdO	181	41	104	36	0
He-sdOB	135	40	47	48	0
He-sdB	17	13	3	1	0

of 27 EHe stars owing mainly to our inclusion of recent discoveries from SALT (Jeffery et al. 2021). On comparison of the population classifications for EHes, both papers agree on memberships for the thin disk and bulge stars. Tisserand et al. (2023) did not identify any EHes in the halo, with the possible exception of V2205 Oph. We classify V2205 Oph as a halo star (Fig. 2) on the basis of its high eccentricity ( $0.57 \pm 0.07$ ) and  $R_a$  ( $9.39 \pm 0.53$  kpc). 3 halo stars in our sample (BD +37 1977, EC 19529–4430 and EC 20236–5703) were not included by Tisserand et al. (2023). 4 stars, V2076 Oph, CoD –46 11775, BD +10 2179 and CoD –48 10153, are classified as thick disk by Tisserand et al. (2023). We classify V2076 Oph as thin disk because of its small  $Z_{\max} = 0.86 \pm 0.03$  kpc. CoD –46 11775 lies in the region that we have defined for the bulge ( $X = -3.59^{+0.17}_{-0.21}$  kpc,  $Y = -1.32^{+0.05}_{-0.06}$  kpc,  $Z = -0.78^{+0.03}_{-0.03}$  kpc). Although BD +10 2179 falls within the thick disk region in the Toomre diagram, its high eccentricity ( $0.53 \pm 0.02$ ) and  $R_a$  ( $10.59 \pm 0.15$  kpc) make it more likely to be a halo star. Finally, CoD –48 10153 falls outside the thick disk regime in the Toomre diagram. However, its highly eccentric orbit ( $0.51 \pm 0.02$ ) and a very low Galactic rotational velocity ( $V = 0.9^{+11.8}_{-15.9}$  km s $^{-1}$ ) clearly make it a halo star.

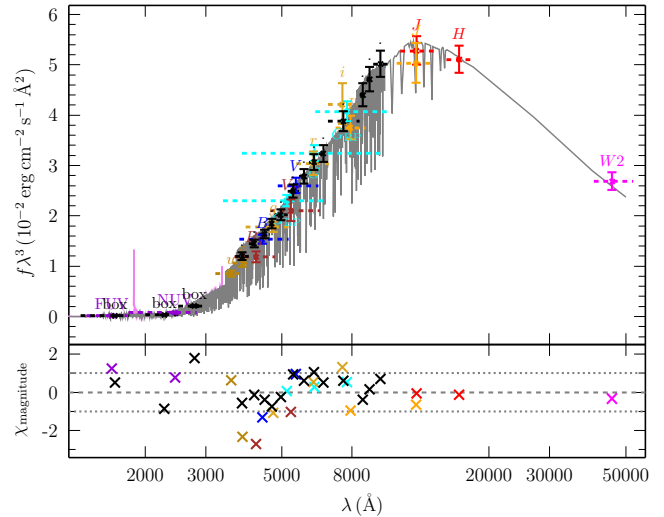
### 4.3 Statistics.

Table 3 compares the numbers of stars classified as thin or thick disk, halo or bulge stars within various classes of hydrogen-deficient star. Five additional subclasses have been classified in exactly the same way as the EHes. Of these, the helium-rich subdwarfs (He-sdB, He-sdOB, He-sdO) are intrinsically fainter than the other classes. The absence of bulge stars in these classes reflects the fact that they are not represented in our sample at such distances. O(He) and PG1159 subclasses were also considered, but are too few to provide useful samples.

It is highly significant that the EHe sample includes stars from the thin disk, the thick disk, the halo and the bulge. We shall return to this in § 5.

Given the sample sizes, the distributions of RCB, HdC and He-sdO stars amongst the four components are not significantly different from that of the EHes. They are dominated by thick disk stars, with thin disk, halo and bulge stars roughly in the ratio 23:53:20:4. The HdC sample shows the largest departure from this ratio, but is roughly consistent given the sample size. The He-sdO sample is 7 times larger than the EHe sample. Thus, the hypothesis that EHe stars may be connected to the RCB, HdC and He-sdO classes cannot be excluded.

The He-sdB sample is heavily dominated by thin disk stars, but the sample size is small. The He-sdOB sample is balanced across thin disk, thick disk and halo and is 4 times larger than the EHe sample. It therefore appears that the He-sdB and He-sdOB samples do not share the characteristics of the EHe and He-sdO samples. The helium-rich subdwarf samples can be further subdivided into, *inter*



**Figure 9.** SED fit from the broadband photometry of V2244 Oph with  $T_{\text{eff}} = 12750$  K (upper panel). The grey line shows the best-fit model SED. The lower panel shows the residuals. Photometry is taken from: Bianchi et al. (2017)(FUV,NUV), Høg et al. (2000)(B<sub>T</sub>,V<sub>T</sub>), Henden et al. (2015)(B,V), Riello et al. (2021)(G<sub>BP</sub>, G, G<sub>RP</sub>), Onken et al. (2019)(u,v,g,r,i,z), Denis (2005)(I,J), Cutri et al. (2003)(J,H) and Schlafly et al. (2019)(W2).

*alia*, intermediate helium-rich and extreme-helium rich subclasses (Jeffery et al. 2021). Detailed analysis of these classes will therefore be deferred.

## 5 LUMINOSITIES AND RADII

One method to derive the luminosity is to obtain the absolute visual magnitude (S. 3.3), and then to obtain the absolute bolometric magnitude by applying a bolometric correction (BC). Since commonly used values for the BC (Weidmann & Bues 1967; Lang 1974; Martins et al. 2005; Nieva 2013) are derived from hydrogen-rich stars, these might not be applicable to hydrogen-deficient stars. An alternative method is to deduce the angular diameter of the star ( $\theta$ ) from the spectral energy distribution (SED), and thence to obtain the actual diameter by multiplying by the distance. If the effective temperature is known, the luminosity follows. In order to apply this method, a theoretical energy distribution from a model atmosphere is convolved with an extinction function and scaled to fit the observed SED. Principal unknowns are the effective temperature of the model atmosphere  $T_{\text{eff}}$ , the extinction coefficient  $E_{(B-V)}$  and  $\theta$ . Other parameters which affect the theoretical model include surface gravity, metallicity and microturbulent velocity. In general these cannot be determined from the SED and must be selected by some other means.

Photometric observations from a number of sources were used to fit the SED of the EHe stars using the model-atmosphere fitting tool ISIS<sup>4</sup> (Heber et al. 2018). These sources include Høg et al. (2000), Cutri et al. (2003, 2021), Denis (2005), McMahon et al. (2013), Henden et al. (2015), Kilkenney et al. (2016), (Bianchi et al. 2017), Schlafly et al. (2018, 2019), Onken et al. (2019), Magnier et al. (2020), Drlica-Wagner et al. (2021), Riello et al. (2021). The

<sup>4</sup> <http://www.sternwarte.uni-erlangen.de/gitlab/irrgang/stellar.git>



**Table 4.** Atmospheric parameters, extinction, magnitudes, luminosities and radii for Extreme Helium stars, ordered by effective temperature. The sample has been divided into those stars with  $L > 2500 L_{\odot}$  above and those with  $L < 2500 L_{\odot}$  below. The sources cited for  $T_{\text{eff}}$  are also sources for  $\log g$  and extinction  $E_{(B-V)}$ , where available. ‘\*’ indicates a missing error for temperature or gravity; we assume  $\pm 2\%$  for temperature and  $\pm 0.25$  for  $\log g$ . † indicates an extinction estimated from Schlegel et al. (1998). G and V magnitudes are from Gaia Collaboration et al. (2023). Masses  $M_L$  and  $M_g$  obtained from the  $M_c - L_s$  relation for helium-shell burning are shown for the high luminosity stars (Fig. 13). The three low-gravity low-luminosity stars from Fig. 13 are also shown in parenthesis.

Star	$T_{\text{eff}}$ (K)	$E_{(B-V)}$	G (mag)	V (mag)	Luminosity ( $\log L_{\odot}$ )	$\log g$ ( $\text{cm s}^{-2}$ )	Radius ( $R_{\odot}$ )	$M_L$ $M_{\odot}$	$M_g$ $M_{\odot}$
NO Ser	11750±250 <sup>1</sup>	0.498±0.010	10.11	10.25	3.60 <sup>+0.15</sup> <sub>-0.01</sub>	2.30±0.40	15.30 <sup>+2.07</sup> <sub>-0.50</sub>	0.60 <sup>+0.03</sup> <sub>-0.01</sub>	0.53 <sup>+0.05</sup> <sub>-0.04</sub>
V2244 Oph	12750±250 <sup>1</sup>	0.500±0.020	10.85	10.94	3.81 <sup>+0.22</sup> <sub>-0.02</sub>	1.75±0.25	16.70 <sup>+3.80</sup> <sub>-0.91</sub>	0.66 <sup>+0.05</sup> <sub>-0.01</sub>	0.67 <sup>+0.08</sup> <sub>-0.06</sub>
PV Tel	13750±400 <sup>3</sup>	0.130±0.010	9.23	9.26	3.83 <sup>+0.17</sup> <sub>-0.06</sub>	1.60±0.25	14.60 <sup>+2.17</sup> <sub>-0.19</sub>	0.64 <sup>+0.04</sup> <sub>-0.01</sub>	0.76 <sup>+0.13</sup> <sub>-0.08</sub>
LSS 99	15330±500 <sup>4</sup>	0.877±0.038	12.05	12.27	4.03 <sup>+0.22</sup> <sub>-0.22</sub>	1.90±0.25	14.80 <sup>+2.99</sup> <sub>-0.98</sub>	0.69 <sup>+0.08</sup> <sub>-0.05</sub>	0.71 <sup>+0.10</sup> <sub>-0.06</sub>
LSS 4357	16130±500 <sup>4</sup>	0.628±0.040	12.43	12.54	3.84 <sup>+0.30</sup> <sub>-0.05</sub>	2.00±0.25	10.90 <sup>+3.25</sup> <sub>-1.10</sub>	0.65 <sup>+0.08</sup> <sub>-0.01</sub>	0.70 <sup>+0.10</sup> <sub>-0.06</sub>
V1920 Cyg	16300±900 <sup>3</sup>	0.310±0.020	10.26	10.30	3.94 <sup>+0.19</sup> <sub>-0.12</sub>	1.70±0.35	11.70 <sup>+1.38</sup> <sub>-0.35</sub>	0.67 <sup>+0.06</sup> <sub>-0.03</sub>	0.89 <sup>+0.36</sup> <sub>-0.16</sub>
CoD -46 11775	18300±400 <sup>3</sup>	0.161±0.015	11.17	11.20	3.57 <sup>+0.15</sup> <sub>-0.22</sub>	2.20±0.20	6.20 <sup>+0.72</sup> <sub>-1.28</sub>	0.61 <sup>+0.03</sup> <sub>-0.03</sub>	0.71 <sup>+0.08</sup> <sub>-0.05</sub>
EC 19529-4430	18540±90 <sup>6</sup>	0.050±0.012 <sup>†</sup>	11.77	11.81	3.41 <sup>+0.34</sup> <sub>-0.14</sub>	3.42±0.04	5.00 <sup>+2.21</sup> <sub>-0.86</sub>	0.57 <sup>+0.06</sup> <sub>-0.02</sub>	0.49 <sup>+0.01</sup> <sub>-0.01</sub>
V2205 Oph	20277±550 <sup>7</sup>	0.300±0.040	10.48	10.51	4.28 <sup>+0.21</sup> <sub>-0.20</sub>	2.55±0.10	11.60 <sup>+1.85</sup> <sub>-2.27</sub>	0.78 <sup>+0.11</sup> <sub>-0.08</sub>	0.66 <sup>+0.02</sup> <sub>-0.02</sub>
LSS 5121	29772±1830 <sup>7</sup>	0.650±0.020	13.16	13.23	3.91 <sup>+0.32</sup> <sub>-0.01</sub>	3.00±0.50	3.40 <sup>+0.93</sup> <sub>-0.39</sub>	0.66 <sup>+0.10</sup> <sub>-0.01</sub>	0.77 <sup>+0.30</sup> <sub>-0.14</sub>
V2076 Oph*	34000±680 <sup>13</sup>	0.450±0.020	9.79	9.82	4.20 <sup>+0.11</sup> <sub>-0.04</sub>	2.80±0.25	3.65 <sup>+0.38</sup> <sub>-0.07</sub>	0.75 <sup>+0.04</sup> <sub>-0.02</sub>	1.10 <sup>+0.53</sup> <sub>-0.25</sub>
BD +37 442*	48000±960 <sup>15</sup>	0.090±0.002 <sup>†</sup>	9.94	10.01	3.72 <sup>+0.10</sup> <sub>-0.07</sub>	4.00±0.25	1.06 <sup>+0.10</sup> <sub>-0.07</sub>	0.62 <sup>+0.02</sup> <sub>-0.02</sub>	0.67 <sup>+0.09</sup> <sub>-0.06</sub>
BD +37 1977*	48000±960 <sup>15</sup>	0.030±0.004 <sup>†</sup>	10.13	10.21	3.96 <sup>+0.12</sup> <sub>-0.13</sub>	4.00±0.25	1.39 <sup>+0.16</sup> <sub>-0.17</sub>	0.68 <sup>+0.03</sup> <sub>-0.03</sub>	0.67 <sup>+0.09</sup> <sub>-0.06</sub>
FQ Aqr	8750±250 <sup>1</sup>	0.100±0.020	9.47	9.51	2.93 <sup>+0.14</sup> <sub>-0.14</sub>	0.75±0.25	12.90 <sup>+1.13</sup> <sub>-1.46</sub>	$\left(0.51^{+0.02}\right)$ <sub>-0.01</sub>	$\left(0.80^{+0.16}\right)$ <sub>-0.1</sub>
LS IV -14 109	9500±250 <sup>1</sup>	0.340±0.050	10.99	11.08	2.61 <sup>+0.12</sup> <sub>-0.13</sub>	0.90±0.20	7.50 <sup>+0.49</sup> <sub>-0.66</sub>	$\left(0.48^{+0.01}\right)$ <sub>-0.01</sub>	$\left(0.79^{+0.11}\right)$ <sub>-0.08</sub>
CoD -48 10153	10600±250 <sup>2</sup>	0.450±0.040	11.33	11.44	3.04 <sup>+0.17</sup> <sub>-0.18</sub>	1.00±0.50	10.00 <sup>+1.35</sup> <sub>-1.62</sub>	$\left(0.52^{+0.02}\right)$ <sub>-0.02</sub>	$\left(0.85^{+0.85}\right)$ <sub>-0.21</sub>
HD 124448	15800±400 <sup>3</sup>	0.092±0.010	9.94	9.97	2.82 <sup>+0.08</sup> <sub>-0.10</sub>	2.10±0.25	3.43 <sup>+0.15</sup> <sub>-0.22</sub>		
BD +10 2179	17300±300 <sup>5</sup>	0.023±0.001	9.92	9.97	3.11 <sup>+0.15</sup> <sub>-0.14</sub>	2.80±0.10	4.00 <sup>+0.55</sup> <sub>-0.50</sub>		
V652 Her	20950±70 <sup>8</sup>	0.060±0.010	10.51	10.56	2.78 <sup>+0.09</sup> <sub>-0.06</sub>	3.46±0.05	1.88 <sup>+0.17</sup> <sub>-0.14</sub>		
BX Cir	23390±90 <sup>9</sup>	0.239±0.008	12.54	12.57	3.13 <sup>+0.15</sup> <sub>-0.04</sub>	3.38±0.02	2.24 <sup>+0.40</sup> <sub>-0.11</sub>		
GALEX J184559.8-413827	26170±750 <sup>10</sup>	0.075±0.001 <sup>†</sup>	14.57	14.62	2.74 <sup>+0.18</sup> <sub>-0.22</sub>	4.22±0.10	1.02 <sup>+0.31</sup> <sub>-0.08</sub>		
EC 20236-5703	26380±130 <sup>6</sup>	0.055±0.012 <sup>†</sup>	14.75	14.80	2.26 <sup>+0.20</sup> <sub>-0.06</sub>	4.14±0.05	0.66 <sup>+0.14</sup> <sub>-0.06</sub>		
LS IV+6 2	31800±800 <sup>11</sup>	0.210±0.020	12.12	12.16	2.85 <sup>+0.13</sup> <sub>-0.05</sub>	4.05±0.10	0.87 <sup>+0.09</sup> <sub>-0.05</sub>		
PG 1415+492	32200±250 <sup>12</sup>	0.011±0.012 <sup>†</sup>	14.27	14.34	2.21 <sup>+0.08</sup> <sub>-0.10</sub>	4.20±0.10	0.41 <sup>+0.03</sup> <sub>-0.04</sub>		
EC 20111-6902	34100±110 <sup>6</sup>	0.036±0.012 <sup>†</sup>	15.84	15.87	2.28 <sup>+0.61</sup> <sub>-0.96</sub>	5.68±0.04	0.39 <sup>+0.39</sup> <sub>-0.26</sub>		
BPS CS 22940-0009	34970±370 <sup>14</sup>	0.052±0.012 <sup>†</sup>	13.97	14.03	2.26 <sup>+0.08</sup> <sub>-0.11</sub>	4.79±0.17	0.37 <sup>+0.02</sup> <sub>-0.04</sub>		
GALEX J191049.5-441713	39690±90 <sup>6</sup>	0.085±0.006 <sup>†</sup>	12.93	12.98	2.58 <sup>+0.11</sup> <sub>-0.04</sub>	5.47±0.03	0.42 <sup>+0.05</sup> <sub>-0.02</sub>		

1: Pandey et al. (2001), 2: Pandey & Reddy (2006), 3: Pandey et al. (2006), 4: Jeffery et al. (1998), 5: Kupfer et al. (2017), 6: Jeffery et al. (2021), 7: Jeffery et al. (2001a), 8: Jeffery et al. (2001b), 9: Woolf & Jeffery (2002), 10: Jeffery (2017), 11: Jeffery (1998), 12: Ahmad & Jeffery (2003) 13: Rauch (1996), 14: Snowden et al. (2022), 15: Jeffery & Hamann (2010)

theoretical spectra used for the fits were taken from grids of line-blanketed model atmospheres computed in local thermodynamic equilibrium with STERNE (Behara & Jeffery 2006). The model grid used for each star was chosen according to the measured metallicity and microturbulence, where available, or on the basis of the similarity of the star’s optical spectrum to those of other EHeS.

ISIS allows us to solve for several parameters at once, or to keep some fixed and solve for others. For hot stars,  $T_{\text{eff}}$  and  $E_{(B-V)}$  are almost degenerate, so free solutions for both are difficult to control (cf. Jeffery et al. 2001a). For consistency,  $T_{\text{eff}}$  was fixed to the most recent value obtained from optical spectroscopy wherever possible. ISIS then solved for  $E_{(B-V)}$  and  $\theta$ . Hence, we deduce the radius

$$R_{\star} = \theta d/2 \quad (7)$$

and the luminosity

$$\frac{L_{\star}}{L_{\odot}} = \left(\frac{R_{\star}}{R_{\odot}}\right)^2 \left(\frac{T_{\text{eff}}}{T_{\text{eff}\odot}}\right)^4. \quad (8)$$

These values have been computed for the EHe stars and are given in Table 4 along with published values for the effective temperatures ( $T_{\text{eff}}$ ), surface gravities ( $\log g$ ) and extinction coefficients ( $E_{(B-V)}$ ).  $T_{\text{eff}}$  and  $\log g$  have been taken from the most recent spectroscopic analyses of optical spectra wherever possible and the sources are cited in Table 4. For measurements that do not have a published error, we have assumed an error of  $\pm 2\%$  for temperature and  $\pm 0.25$  dex for  $\log g$ . Some measurements cited in Table 4 have very small error; these are taken to be formal errors. To partially account for likely larger systematic errors, minimum errors of  $\pm 1\%$  and 0.05

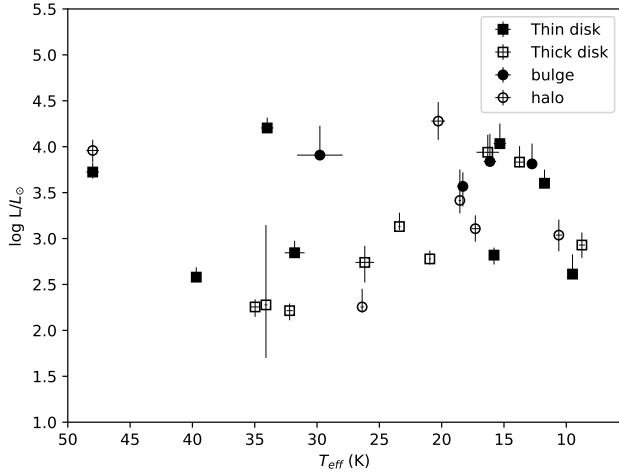


**Figure 10.** Luminosities of EHe stars derived from *Gaia* distances and SED-based angular diameters as a function of effective temperature. Symbols represent the population assignments given in Table 4 (see key).

dex are adopted for  $T_{\text{eff}}$  and  $\log g$  respectively for propagation. Figure 9 shows an example of an SED fit for the cool EHe V2244 Oph. None of the SED fits show any evidence for an infra-red excess that might indicate an unseen cool companion or a dust shell.

Since we have the surface gravity and radius for each star, we may in principle deduce the mass

$$M_{\star} = \frac{g}{G} R_{\star}^2. \quad (9)$$

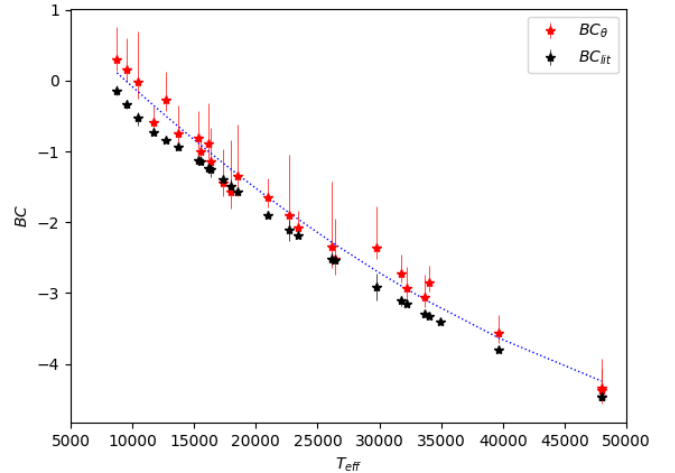
In practice, whilst the errors in radius are usually smaller than  $\pm 10\%$ , their contribution doubles in the derivation of mass and the errors in surface gravity are mostly between  $\pm 25\%$  and  $\pm 80\%$ . Consequently, the mass errors ( $1\sigma$ ) exceed 100% for half of the EHe sample, and are less than 50% for only 5 EHe stars. The deduced masses run from  $0.02^{+0.015}_{-0.003} - 2.71^{+3.62}_{-5.44} M_{\odot}$  and 12 cluster between 0.2 and  $0.5 M_{\odot}$ . In view of the errors and the spread, we attach little confidence to these data. Likely reasons include the difficulty of measuring surface gravities and the presence of large amplitude pulsations in these luminous stars; unless angular radii and surface gravities are obtained at equivalent phases in approximately hydrostatic equilibrium, significant systematic errors will occur. The issues are examined in detail for the case of V652 Her by Jeffery et al. (2022).

Figure 10 shows the luminosities as a function of effective temperature. This suggests that EHe stars may be divided into two luminosity groups, with a dividing line at  $L \approx 2500 L_{\odot}$ . The more luminous group  $L \approx 2500 - 20000 L_{\odot}$  shows roughly similar luminosity over the entire temperature range. The less luminous group  $L \approx 100 - 2500 L_{\odot}$  shows a progression towards lower luminosity with increasing temperature. The two groups are also identified in Table 4. It is significant that both groups include stars from the thin disk, the thick disk, and the halo.

### 5.1 Bolometric correction for EHe stars

To determine whether the bolometric corrections available in literature for stars of these temperature ranges could be applicable to EHe stars, we converted the SED luminosities to  $M_{\text{bol}\star}$  using

$$M_{\text{bol}\star} = -2.5 \log_{10} \left( \frac{L_{\star}}{L_{\odot}} \right) + M_{\text{bol}\odot} \quad (10)$$



**Figure 11.** Comparison between BC adopted from Weidemann & Bues (1967), Lang (1974), Martins et al. (2005) and Nieva (2013) ( $BC_{\text{lit}}$ ) and BC obtained using the spectral energy distributions ( $BC_{\theta}$ ) of the EHe stars in the temperature range 8750 K - 48000 K. The blue dotted line depicts a low order polynomial fit to the data.

and then compared with the absolute visual magnitude from Eq. 3 to obtain the bolometric correction

$$BC = M_{\text{bol}\star} - M_V. \quad (11)$$

Figure 11 compares the EHe bolometric corrections with the bolometric corrections from Weidemann & Bues (1967); Lang (1974); Martins et al. (2005); Nieva (2013). The correction for helium stars seems to be more positive than the literature values by about 0.3 mag. This is probably due to the absence of Balmer line and continuum absorption in the EHe stars. The BC for EHe stars can be expressed as a function of  $T_{\text{eff}}$  by the polynomial fit shown in Fig. 11:

$$BC = 1.59 - 1.79 (T_{\text{eff}}/10^4) + 0.122 (T_{\text{eff}}/10^4)^2. \quad (12)$$

This correction can also be used to obtain luminosities for stars with insufficient photometric data for an SED fit.

## 6 INFERENCES ON EVOLUTION, AGE, AND NUMBERS

With spatial and kinematic data, as well as luminosities, we are in a position to discuss the age, origin and evolution of EHe stars.

Using their distribution and radial velocity in the Galactic frame, Drilling & Hill (1986) argued that EHe stars belong to the Galactic bulge. Iben & Tutukov (1985) derived a scale height 1700 pc for the EHe star population, which would be commensurate with a thick disk population. The current analysis shows that EHe stars include stars representative of all the major Galactic populations, including the thin and thick disk as well as the bulge and halo. Thus EHe stars must arise from star formation at many epochs of Galactic evolution. The *Gaia* analysis also shows that EHe stars form two luminosity groups, implying more than one formation channel.

### 6.1 Evolution

It has been proposed that RCB and EHe stars form as a result of the merger of two white dwarfs (WDs) (Webbink 1984; Saio & Jef-

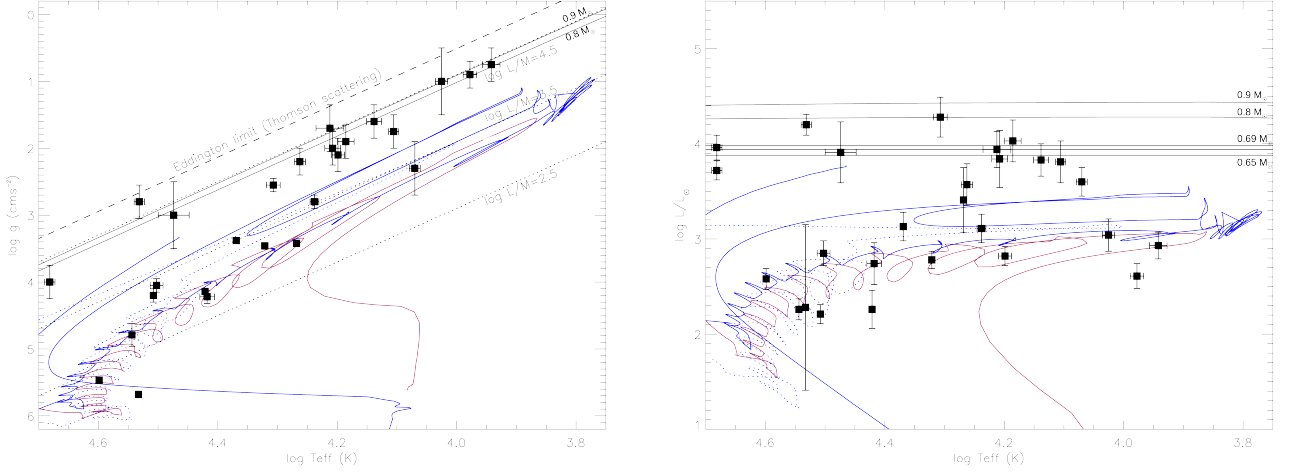


**Figure 12.** A comparison of the post-merger evolution of double white dwarfs with the observed properties of Extreme Helium stars. Left: the Kiel ( $g - T_{\text{eff}}$ ) diagram. The black dotted lines indicate equal  $L/M$  ratio as marked. The grey lines show the post-merger evolution tracks for models of CO+He WD mergers from Saio & Jeffery (2002) with product masses  $0.6 + 0.2$  and  $0.6 + 0.3 M_{\odot}$ . The blue lines show tracks for He+He WD mergers from Saio & Jeffery (2000) with the dotted line corresponding to  $0.3 + 0.2 M_{\odot}$  and solid corresponding to  $0.4 + 0.3 M_{\odot}$ . The red line shows the track for a  $0.3 + 0.25 M_{\odot}$  He+He WD merger from Zhang & Jeffery (2012a). Right: The Hertzsprung-Russell ( $L - T_{\text{eff}}$ ) diagram, plotted with the same evolution tracks. Dark grey lines show CO+He WD post-merger tracks from Schwab (2019) with final masses  $0.69$ ,  $0.67$  and  $0.65 M_{\odot}$ .

ery 2002). Post-merger evolution depends on the nature of the WDs involved; for example:

- He+He WD  $\rightarrow$  ??  $\rightarrow$  EHe  $\rightarrow$  He-sdO  $\rightarrow$  DO WD (Saio & Jeffery 2000; Zhang & Jeffery 2012a)<sup>5</sup>
- He+He WD  $\rightarrow$  ??  $\rightarrow$  EHe  $\rightarrow$  He-sdO  $\rightarrow$  RCB  $\rightarrow$  EHe  $\rightarrow$  He-sdO<sup>+</sup>  $\rightarrow$  O(He)  $\rightarrow$  DO WD (Zhang & Jeffery 2012b)
- Co+He WD  $\rightarrow$  RCB  $\rightarrow$  EHe  $\rightarrow$  He-sdO<sup>+</sup>  $\rightarrow$  O(He)  $\rightarrow$  DO WD (Webbink 1984; Saio & Jeffery 2002; Zhang et al. 2014; Schwab 2019)

The middle sequence may be impossible to distinguish from either the first or last sequence, having the characteristics of both. It is not clear what the immediate product of a He+He WD merger will be; hence '??' above. Its lifetime will be short, being only the lifetime of a helium shell-flash cycle at the start of core helium burning. It may well be a cool EHe or HdC star. In contrast, the lifetime of the immediate He+CO WD merger product is relatively long, being the lifetime for the helium-burning shell to consume available fuel above the carbon-oxygen core; this may be some  $0.3 - 0.4 M_{\odot}$ . It is reasonable that these may be RCB or HdC stars.

Given the two EHe luminosity groups, it seems likely that the EHe sample includes post-merger products from both CO+He WD binaries and He+He WD binaries. The lower luminosity EHe ( $L > 2500 L_{\odot}$ ) and He-sdO's have already been identified with the He+He WD merger sequence (Saio & Jeffery 2000; Zhang & Jeffery 2012a). The higher luminosity EHe ( $L > 2500 L_{\odot}$ ) are identified with the merger of a CO+He WD binary (Saio & Jeffery 2002; Zhang et al. 2014; Schwab 2019), evolving via the low gravity hot sdO domain (He-sdO<sup>+</sup> and O(He) stars) to become hot WDs. Clayton et al. (2007) established that the cooler RCBs lie on the same pathway. A strict boundary cannot be drawn because it is possible to form He+He systems which are more massive than the lightest

<sup>5</sup> Iben (1990) proposed that a He+He WD merger would produce an sdB star; in fact, Iben's model cannot account for the classical hydrogen-rich sdB stars but is equivalent to this sequence.

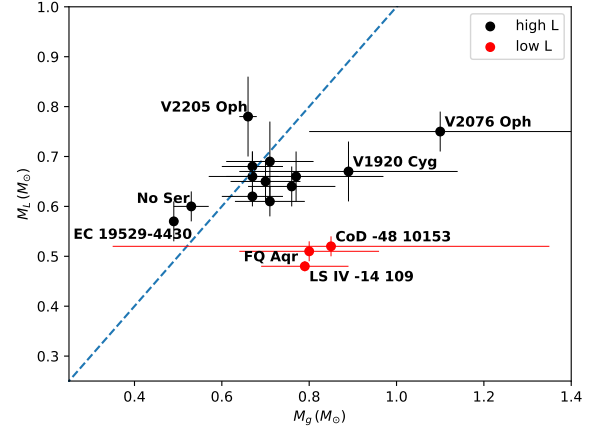


**Figure 13.** EHe masses derived from observed luminosities ( $M_L/M_{\odot}$ ) and surface gravities ( $M_g/M_{\odot}$ ) and the  $M_c - L_s$  relation appropriate for CO+He WD mergers (Jeffery 1988).

CO+He systems, and because the former can emulate the evolution of the latter after completion of core helium burning (Zhang & Jeffery 2012b).

Figure 12 compares post-merger tracks for both He+He and CO+He WD mergers with the *Gaia*-derived luminosities as well as the spectroscopic surface gravities of the EHe.

The intrinsically brighter EHe have luminosities consistent with post-merger tracks for CO+He WDs in the  $0.65 - 0.9 M_{\odot}$  range, as identified by Saio & Jeffery (2002); Zhang et al. (2014); Schwab (2019). For these, evolution proceeds via contraction at constant luminosity, approximately on a thermal timescale. The luminosity reflects the stars' masses, as indicated by the core-mass shell-luminosity ( $M_c - L_s$ ) relation for helium-shell burning stars (Jeffery 1988) which we have verified against the Saio & Jeffery (2002) and Schwab (2019) evolution tracks.

Systems with  $L < 2500 L_{\odot}$  are more likely to have been produced in He+He systems with total masses  $\leq 0.7 M_{\odot}$ . Whilst initially bright after shell-helium ignition, these stars contract and dim as the helium-burning shell burns inwards towards the core, eventually reaching the helium main-sequence.

Estimates for the mass of each EHe star can be obtained from theoretical evolution tracks (Fig. 12) or from the Jeffery (1988)  $M_c - L_s$  relation by separately comparing with the observed surface gravity to give mass  $M_g$ , and luminosity to give  $M_L$ .

Values of  $M_L$  and  $M_g$  obtained from the  $M_c - L_s$  relation for high- $L$  EHes ( $L > 2500 L_{\odot}$ ) are shown in Table 4 and compared in Fig. 13. V2244 Oph, LSS 99, LSS 4357, BD+37 442 and BD+37 1977 have  $M_g$  and  $M_L$  in good agreement between 0.62 and 0.71  $M_{\odot}$ . LSS 5121, CoD -46 11775 and PV Tel have  $M_L$  in the range 0.59 – 0.66  $M_{\odot}$ , but  $M_g$  in the range 0.71 – 0.76  $M_{\odot}$ . NO Ser and EC 19529–4430 have  $M_L$  in the range 0.57 – 0.60  $M_{\odot}$ , but markedly lower  $M_g$ . For V2205 Oph,  $M_g$  is also too low. V1920 Cyg and V2076 Oph have  $M_g$  substantially higher than the corresponding  $M_L$ . Overall, the *Gaia*+SED luminosities support masses for post-merger He+CO white dwarfs in the range 0.57 – 0.78  $M_{\odot}$ . Significant differences between  $M_L$  and  $M_g$  should be examined in more detail, particularly with respect to surface gravity and extinction.

FQ Aqr, LS IV-14 109 and CoD -48 10153 are included in Fig. 13 because their surface gravities suggest a high luminosity, which is not supported by the *Gaia*+SED measurements. The low- $L$  EHes ( $L < 2500 L_{\odot}$ ) lie well below the luminosities predicted for CO+He mergers. Masses cannot be derived from the post-merger evolution tracks for He+He WDs since, for a given class of model, these are degenerate in  $g$  (and  $L$ ) during contraction toward the helium main-sequence (Zhang & Jeffery 2012a). Moreover, loops associated with helium-shell flashes broaden the tracks by more than any difference caused by a change in mass.

According to Tisserand et al. (2020), the cool group of RCB stars represents about 2/3 the entire RCB sample, but is under-represented in atmospheric analyses. With 118 Galactic RCB stars now known (Tisserand et al. 2020), substantial numbers of accurate  $T_{\text{eff}}$ ,  $g$  measurements for stars within 10 kpc could transform Fig. 12 into a tool that will place useful constraints on evolution models and stellar physics. Additionally, with precise bolometric corrections for a larger temperature range, Fig. 12 would be expanded to include other sets of helium stars, thereby shedding more light on evolutionary pathways.

## 6.2 Age

The defining timescales for double WD mergers are those of the progenitor binary followed by the orbital-decay time of the double WD system. Post-merger evolution timescales are comparatively short, so all current EHes probably formed within the last  $10^4 - 10^6$  y. From a composite model for the star-formation history of the Galaxy, Yu & Jeffery (2011) argue that the majority (> 95%) of CO+He double WDs currently alive in the Galactic disc were formed between 4 and 10 Gyr before the present epoch. However, the fraction of these that contribute to the present-day CO+He WD merger rate is dominated by star formation between 1 and 3 Gyr before the present. Supporting this, Zhang et al. (2014) show that, for a single starburst, CO+He WD mergers peak some 1 Gyr after the starburst, declining exponentially by a factor 10 over 3 Gyr, but then remaining steady up to at least 10 Gyr after the starburst (i.e. at  $\approx 1/10$  the rate for  $\approx 10 \times$  the time). Thus the majority of EHes should come from relatively recent star formation. This is supported by the fact that

**Table 5.** Relative frequency of double white dwarf binary mergers by Galactic population and binary white dwarf class at the current epoch based on Yu & Jeffery (2010, 2011) and normalised to 100  $\text{yr}^{-1}$ . The associated total rate for the Galaxy over all merger types is  $\sim 2.8 \times 10^{-3} \text{ yr}^{-1}$ .

White Dwarfs	Galaxy	Thin Disk	Thick Disk	Halo	Bulge
He+He	34	17	1	16	8
CO+He	14	7	1	5	2
CO+CO	46	22	2	10	5
ONeMG+X	6	3	0	1	1
All	100	49	4	32	15

2/3 of the sample belong to the thin (8) and thick (9) disks (Table 3). However, the tail of the distribution, which formed up to 10 Gyr or more in the past, will continue to provide a significant number of recent CO+He WD mergers in all Galactic populations.

## 6.3 Numbers

Predictions for relative numbers of double white dwarf mergers in different populations have been derived in many studies using the methods of binary star population synthesis (BSPS) (e.g. Yu & Jeffery 2010, 2011; Zhang et al. 2014). Table 5 shows the relative merger rates obtained by combining the rates per Galactic component (Yu & Jeffery 2010, Table 2) with the rates per merger type (Yu & Jeffery 2011, Tables 2,3), assuming a quasi-exponential star-formation history for the thin and thick disks, and an instantaneous star-formation history for the bulge and halo. These statistics include both stable and unstable mergers (Zhang et al. 2014, Figs. 1,24). Only a subset of the latter will give rise to EHe stars, a supernova explosion being an alternative for the most massive mergers. There are significant differences between merger-rate predictions. Yu & Jeffery (2011, Fig. 11) and Zhang et al. (2014, Fig. 23) show the same quantities, with qualitatively similar, but quantitatively different, results. This is not the place to explore the particulars of different BSPS implementations. Rather, the intent of Table 5 is to compare the contributions of He+He and CO+He merger channels and their parent populations with observed EHe numbers (Table 3 and Figs. 10,12).

Ideally, merger rates should be combined with the lifetimes of post-merger products to obtain number densities, and adjusted for completeness in order to compare with observed numbers. However, even without adjustment, Table 5 clearly shows a shortage of predicted WD mergers in the thick disk relative to other locations when compared with the observed numbers of EHes, RCBs and He-sdOs (Table 3). Yu & Jeffery (2010, Table 1) used a model in which the thick disk has 5% the mass of the thin disk, whilst Bensby et al. (2014, Table A.1) cite a ratio closer to 11%, but this cannot account for all of the shortage in predicted numbers. The observed numbers suggest the delay-time distribution for He+He and CO+He WD mergers is too low in the 3 - 10 Gyr range, and hence that the distribution of initial periods of post-common-envelope double WDs is too heavily weighted to short periods. Adjusting the common-envelope ejection efficiency in binary star evolution models to produce more widely separated post-common-envelope systems could ameliorate the problem. Another explanation could be that, since EHes are rare but luminous, they are seen at greater distances in the thick disk than in the more heavily obscured thin disk; is there a missing population of EHes close to the Galactic plane? We note that the kick velocity imparted to the survivor of a double white dwarf merger due to the destruction of one component is only a few  $\text{km s}^{-1}$



(Dan et al. 2014) and will have little overall effect on the population assignments.

It has been proposed that EHeS could alternatively follow canonical stellar evolution as stripped post-AGB stars or as the remnant of a late thermal pulse in a post-AGB star (Iben et al. 1983). Whilst neither proposal explains the absence of binaries and the surface chemistries of EHeS, it is useful to compare with the Galactic distribution of other post-AGB stars. A well-defined sample is provided by the planetary nebulae (PNe). PNe with [WC]-type central stars could represent a sequence of late thermal pulse stars (Herwig 2001; Blöcker 2001). PNe in the galactic halo are extremely rare (Clegg 1987, 3 field PNe). Górný et al. (2004) divided the Strasbourg-ESO catalogue of Galactic PNe (Acker et al. 1992) into 263 bulge objects and 878 disk objects. The fraction of [WC]-type PN is similar across both populations at 55/263 for the bulge and 154/878 for the remainder. However, considering selection effects, Górný et al. (2004) concluded that the fraction of [WR] PNe is significantly larger in the bulge than in the disk. The San Pedro Mártir kinematic catalogue (López et al. 2012) divided the Galactic PNe sample into 405 thin disk, 24 thick disk, 17 halo and 155 bulge PNeS. Ali et al. (2013) found roughly equal numbers of PNe in the thin and thick disks. Crudely, the available data suggest a distribution of  $\approx 48:27:1:24$  for the thin disk, thick disk, halo and bulge PNe. Similarly, the Galactic population of AGB stars is dominated by the thin disk and bulge, with a survey of IRAS-selected AGB stars finding only 15/6039 stars having  $|Z| > 2.5$  kpc (Jackson et al. 2002). The larger fraction of halo EHe and other hydrogen-deficient stars (Table 3) contrasts starkly with the deficit of halo PNe and AGB stars. It would appear that halo stars massive enough to produce PNe and, by inference, a late thermal pulse, have long since completed their evolution. In contrast, double white dwarfs in the halo can continue to produce mergers on a timescales commensurate with the age of the Galaxy.

## 7 CONCLUSIONS

*Gaia* DR3 has provided parallaxes and proper motions for hundreds of millions of stars, including extremely rare hydrogen-deficient stars such as R CrB variables, hydrogen-deficient carbon giants, extreme helium stars (EHeS), and helium-rich hot subdwarfs.

In conjunction with the ongoing SALT survey of hydrogen-deficient stars (Jeffery et al. 2021) we have updated the list of known EHeS; the focus of this paper has been to examine their Galactic distribution and kinematics, and hence learn something about their origin, age, and relationship with other classes of hydrogen-deficient star.

The *Gaia* DR3 data have been processed with *galpy* to obtain complete orbital and spatial information for 27 EHeS. We have also analysed comparison samples of 38 RCBs, 8 HdCs, 181 He-sdOs, 135 He-sdOBs and 17 He-sdBs. These data have been used to classify the parent populations for each star. EHeS can clearly be found in all of the thin disk, the thick disk, the halo and the bulge of the Galaxy. The same is true, in similar proportion, for RCBs, HdCs and He-sdOs, but the largest fraction of all four classes are found in the thick disk. EHeS, RCBs and HdCs are luminous and hence have short lifetimes. Their presence in all four components of the Galaxy implies that their progenitor lifetimes must cover a wide range from a few to more than 10 Gyr.

We have combined the *Gaia* DR3 distances with analyses of the EHe spectral energy distributions to obtain radii and luminosities. From the luminosities, we find that the EHeS can be divided into two luminosity groups, with the division at  $\log L/L_{\odot} \approx 3.4$ . Thin

and thick disk and halo populations are all represented in both luminosity groups. The existence and population characteristics of both groups are best understood if:

- EHeS with lower luminosities ( $L < 2500 L_{\odot}$ ) correspond to the post-merger evolution of double white dwarf binaries containing two helium white dwarfs; these are contracting towards the helium main-sequence where they will be observed as He-sdOs, and
- EHeS with higher luminosities ( $L > 2500 L_{\odot}$ ) correspond to the post-merger evolution of double white dwarf binaries containing a carbon-oxygen and a helium white dwarf; these are contracting at roughly constant luminosity to eventually become hot white dwarfs. We have also derived an equation for the bolometric correction appropriate to hydrogen-deficient stars in the effective temperature range 7 000 – 50 000 K.

We have briefly discussed the parent populations for both classes of double white dwarf merger. Binary star population synthesis predicts that double white dwarfs capable of merging at the current epoch should exist in all Galactic populations. However, the predictions favour mergers arising from recent star formation (i.e. thin disk), whereas the statistics favour an older epoch (i.e. thick disk). Further analyses of the He-sdO, RCB and HdC populations will be instructive.

## ACKNOWLEDGMENTS

APM and PM acknowledge studentships from the Armagh Observatory and Planetarium which, in turn, is supported by a core grant from the Northern Ireland Department for Communities. CSJ acknowledges support from the UK Science and Technology Facilities Council via UKRI Grant No. ST/V000438/1.

This work has made use of data from the European Space Agency (ESA) mission *Gaia*<sup>6</sup>, processed by the *Gaia* Data Processing and Analysis Consortium (DPAC)<sup>7</sup>. Funding for the DPAC has been provided by national institutions, in particular the institutions participating in the *Gaia* Multilateral Agreement.

We thank the referee for very helpful comments.

## DATA AVAILABILITY STATEMENT

The astrometric data underlying this article are available in the *Gaia* Archive at ESA and can be accessed via the archive website at [gea.esac.esa.int/archive/](http://gea.esac.esa.int/archive/). All other data are available in the publications cited.

## REFERENCES

- Acker A., Marcout J., Ochsenbein F., Stenholm B., Tyndra R., Schohn C., 1992, The Strasbourg-ESO Catalogue of Galactic Planetary Nebulae. Parts I, II.
- Ahmad A., Jeffery C. S., 2003, *A&A*, **402**, 335
- Ali A., Ismail H. A., Snaid S., Sabin L., 2013, *A&A*, **558**, A93
- Bailer-Jones C. A. L., 2015, *PASP*, **127**, 994
- Bailer-Jones C. A. L., Rybizki J., Fouesneau M., Demleitner M., Andrae R., 2021, *AJ*, **161**, 147
- Behara N. T., Jeffery C. S., 2006, *A&A*, **451**, 643
- Bensby T., Feltzing S., Oey M. S., 2014, *A&A*, **562**, A71
- Bianchi L., Shiao B., Thilker D., 2017, *ApJS*, **230**, 24

<sup>6</sup> [www.cosmos.esa.int/gaia](http://www.cosmos.esa.int/gaia)

<sup>7</sup> [www.cosmos.esa.int/web/gaia/dpac/consortium](http://www.cosmos.esa.int/web/gaia/dpac/consortium)



- Bland-Hawthorn J., Gerhard O., 2016, *ARA&A*, **54**, 529
- Blöcker T., 2001, *Ap&SS*, **275**, 1
- Bovy J., 2011, PhD thesis, New York University
- Bovy J., 2015, *ApJ*, **216**, 29
- Clayton G. C., 1996, *PASP*, **108**, 225
- Clayton G. C., 2012, *J. American Assoc. Var. Star Observers*, **40**, 539
- Clayton G. C., Geballe T. R., Herwig F., Fryer C., Asplund M., 2007, *ApJ*, **662**, 1220
- Clegg R. E. S., 1987, in *European Southern Observatory Conference and Workshop Proceedings*. pp 543–551
- Crawford C. L., et al., 2023, *MNRAS*, **521**, 1674
- Culpan R., Geier S., Reindl N., Pelisoli I., Gentile Fusillo N., Vorontseva A., 2022, *A&A*, **662**, A40
- Cutri R. M., et al., 2003, *VizieR Online Data Catalog*, **2246**
- Cutri R. M., et al., 2021, *VizieR Online Data Catalog*, **p. II/328**
- Dan M., Rosswog S., Brüggen M., Podsiadlowski P., 2014, *MNRAS*, **438**, 14
- Denis C., 2005, *VizieR Online Data Catalog*, **p. B/denis**
- Drilling J. S., Hill P. W., 1986, in *Hunger K., Schönberner D., Kameswara Rao N., eds, Astrophysics and Space Science Library Vol. 128, Hydrogen Deficient Stars and Related Objects, Proceedings of IAU Colloq. 87*. D. Reidel Publishing Co, Dordrecht, p. 499
- Drimmel R., Poggio E., 2018, *Research Notes of the American Astronomical Society*, **2**, 210
- Drlica-Wagner A., et al., 2021, *ApJS*, **256**, 2
- GRAVITY Collaboration et al., 2021, *A&A*, **654**, A22
- Gaia Collaboration et al., 2016, *A&A*, **595**, A1
- Gaia Collaboration et al., 2023, *A&A*, **674**, A1
- Geier S., 2020, *A&A*, **635**, A193
- Górny S. K., Stasińska G., Escudero A. V., Costa R. D. D., 2004, *A&A*, **427**, 231
- Heber U., Irrgang A., Schaffenroth J., 2018, *Open Astronomy*, **27**, 35
- Henden A. A., Levine S., Terrell D., Welch D. L., 2015, in *American Astronomical Society Meeting Abstracts #225*. p. 336.16
- Herwig F., 2001, *ApJ*, **554**, L71
- Høg E., et al., 2000, *A&A*, **355**, L27
- Iben Jr. I., 1990, *ApJ*, **353**, 215
- Iben Jr. I., Tutukov A. V., 1985, *ApJS*, **58**, 661
- Iben Jr. I., Kaler J. B., Truran J. W., Renzini A., 1983, *ApJ*, **264**, 605
- Jackson T., Ivezić Ž., Knapp G. R., 2002, *MNRAS*, **337**, 749
- Jeffery C. S., 1988, *MNRAS*, **235**, 1287
- Jeffery C. S., 1996, in *Jeffery C. S., Heber U., eds, Astronomical Society of the Pacific Conference Series Vol. 96, Hydrogen Deficient Stars*. p. 152
- Jeffery C. S., 1998, *MNRAS*, **294**, 391
- Jeffery C. S., 2017, *MNRAS*, **470**, 3557
- Jeffery C. S., Hamann W. R., 2010, *MNRAS*, **404**, 1698
- Jeffery C. S., Drilling J. S., Heber U., 1987, *MNRAS*, **226**, 317
- Jeffery C. S., Heber U., Hill P. W., Dreizler S., Drilling J. S., Lawson W. A., Leuenhagen U., Werner K., 1996, in *Jeffery C. S., Heber U., eds, Astron. Soc. Pac. Conf. Ser. Vol. 96, Hydrogen Deficient Stars. Astronomical Society of the Pacific, San Francisco*, p. 471
- Jeffery C. S., Hamill P. J., Harrison P. M., Jeffers S. V., 1998, *A&A*, **340**, 476
- Jeffery C. S., Starling R. L. C., Hill P. W., Pollacco D., 2001a, *MNRAS*, **321**, 111
- Jeffery C. S., Woolf V. M., Pollacco D. L., 2001b, *A&A*, **376**, 497
- Jeffery C. S., Karakas A. I., Saio H., 2011, *MNRAS*, **414**, 3599
- Jeffery C. S., Ahmad A., Naslim N., Kerzendorf W., 2015, *MNRAS*, **446**, 1889
- Jeffery C. S., Rao N. K., Lambert D. L., 2020, *MNRAS*, **493**, 3565
- Jeffery C. S., Miszalski B., Snowdon E., 2021, *MNRAS*, **501**, 623
- Jeffery C. S., Montañés-Rodríguez P., Saio H., 2022, *MNRAS*, **509**, 1940
- Kawka A., Vennes S., O’Toole S., Németh P., Burton D., Kotze E., Buckley D. A. H., 2015, *MNRAS*, **450**, 3514
- Kilkenny D., Koen C., Jeffery C. S., Hill N. C., O’Donoghue D., 1999, *MNRAS*, **310**, 1119
- Kilkenny D., Worters H. L., O’Donoghue D., Koen C., Koen T., Hambly N., MacGillivray H., Stobie R. S., 2016, *MNRAS*, **459**, 4343
- Kupfer T., Przybilla N., Heber U., Jeffery C. S., Behara N. T., Butler K., 2017, *MNRAS*, **471**, 877
- Lang K. R., 1974, *Astrophysical formulae : a compendium for the physicist and astrophysicist*. Springer-Verlag: Berlin Heidelberg New York
- Lawson W. A., Kilkenny D., van Wyk F., Marang F., Pollard K., Ryder S. D., 1993, *MNRAS*, **265**, 351
- Lindegren L., et al., 2021, *A&A*, **649**, A4
- López J. A., Richer M. G., García-Díaz M. T., Clark D. M., Meaburn J., Riesgo H., Steffen W., Lloyd M., 2012, *Rev. Mex. Astron. Astrofis.*, **48**, 3
- Luri X., et al., 2018, *A&A*, **616**, A9
- Lynas-Gray A. E., Schönberner D., Hill P. W., Heber U., 1984, *MNRAS*, **209**, 387
- Ma X., Hopkins P. F., Wetzel A. R., Kirby E. N., Anglés-Alcázar D., Faucher-Giguère C.-A., Kereš D., Quataert E., 2017, *MNRAS*, **467**, 2430
- Magnier E. A., et al., 2020, *ApJS*, **251**, 6
- Martin P., 2019, PhD thesis, Trinity College Dublin
- Martin P., Jeffery C. S., 2017, *Open Astronomy*, **26**, 240
- Martin P., Jeffery C. S., Naslim N., Woolf V. M., 2017, *MNRAS*, **467**, 68
- Martins F., Schaerer D., Hillier D. J., 2005, *Astronomy and Astrophysics*, **436**, 1049
- McMahon R. G., Banerji M., Gonzalez E., Kuposov S. E., Bejar V. J., Lodieu N., Rebolo R., VHS Collaboration 2013, *The Messenger*, **154**, 35
- Miyamoto M., Nagai R., 1975, *PASJ*, **27**, 533
- Navarro J. F., Frenk C. S., White S. D. M., 1996, *ApJ*, **462**, 563
- Nieva M. F., 2013, *Astronomy and Astrophysics*, **550**
- Onken C. A., et al., 2019, *Publ. Astron. Soc. Australia*, **36**, e033
- Pandey G., Reddy B. E., 2006, *MNRAS*, **369**, 1677
- Pandey G., Kameswara Rao N., Lambert D. L., Jeffery C. S., Asplund M., 2001, *MNRAS*, **324**, 937
- Pandey G., Lambert D. L., Jeffery C. S., Rao N. K., 2006, *ApJ*, **638**, 454
- Pauli E.-M., Napiwotzki R., Altmann M., Heber U., Odenkirchen M., Kerber F., 2003, *A&A*, **400**, 877
- Przybilla N., Fossati L., Jeffery C. S., 2021, *A&A*, **654**, A119
- Randall S. K., Bagnulo S., Ziegerer E., Geier S., Fontaine G., 2015, *A&A*, **576**, A65
- Rauch T., 1996, in *C. S. Jeffery & U. Heber ed., Astron. Soc. Pac. Conf. Ser. Vol. 96, Hydrogen Deficient Stars. Astron. Soc. Pac., San Francisco*, pp 174–+
- Reid M. J., Brunthaler A., 2020, *ApJ*, **892**, 39
- Reindl N., Rauch T., Werner K., Kruk J. W., Todt H., 2014, *A&A*, **566**, A116
- Riello M., et al., 2021, *Astronomy and Astrophysics*, **649**
- Robin A. C., Reylé C., Derrière S., Picaud S., 2003, *A&A*, **409**, 523
- Saio H., Jeffery C. S., 2000, *MNRAS*, **313**, 671
- Saio H., Jeffery C. S., 2002, *MNRAS*, **333**, 121
- Schlafly E. F., et al., 2018, *ApJS*, **234**, 39
- Schlafly E. F., Meisner A. M., Green G. M., 2019, *ApJS*, **240**, 30
- Schlegel D. J., Finkbeiner D. P., Davis M., 1998, *ApJ*, **500**, 525
- Schwab J., 2019, *ApJ*, **885**, 27
- Snowdon E. J., Scott L. J. A., Jeffery C. S., Woolf V. M., 2022, *MNRAS*, **516**, 794
- Tisserand P., et al., 2020, *A&A*, **635**, A14
- Tisserand P., et al., 2022, *A&A*, **667**, A83
- Tisserand P., Crawford C. L., Soon J., Clayton G. C., Ruiter A. J., Seitzzahl I. R., 2023, *arXiv e-prints*, **p. arXiv:2309.10148**
- Walker H. J., Hill P. W., 1985, *A&AS*, **61**, 303
- Webbink R. F., 1984, *ApJ*, **277**, 355
- Weidemann V., Bues I., 1967, *Z. Astrophys.*, **67**, 415
- Woolf V. M., Jeffery C. S., 2002, *A&A*, **395**, 535
- Yu S., Jeffery C. S., 2010, *A&A*, **521**, A85+
- Yu S., Jeffery C. S., 2011, *MNRAS*, **417**, 1392
- Zhang X., Jeffery C. S., 2012a, *MNRAS*, **419**, 452
- Zhang X., Jeffery C. S., 2012b, *MNRAS*, **426**, L81
- Zhang X., Jeffery C. S., Chen X., Han Z., 2014, *MNRAS*, **445**, 660
- de Bruijne J. H. J., Eilers A.-C., 2012, *A&A*, **546**, A61

## **APPENDIX A: SECONDARY SAMPLE**

The stars in the secondary sample defined in Section 2, numbering 383, include members of various classes of hydrogen-deficient stars and are shown in Table A1. The method used to deduce population membership is the same as that for EHes (Section 4).

**Table A1.** Orbital parameters and Galactic velocities of the secondary sample grouped by class and sorted as in Table 1. The population membership has the same meaning as in Table 2.

Star	$U$	$V$	$W$	$J_z$	$e$	$R_a$	$R_p$	$Z_{\max}$	pop	class
	km s <sup>-1</sup>	km s <sup>-1</sup>	km s <sup>-1</sup>							
V* XX Cam	33.1	238.3	3.9	2227.4	0.10	10.77	8.82	0.07	TH	RCB
V* UX Ant	-257.9	-93.4	85.8	3964.7	0.11	22.98	18.41	7.97	H	RCB
V* UW Cen	-255.2	185.8	16.2	1610.1	0.08	7.68	6.49	1.16	H	RCB
V* Y Mus	-215.5	123.3	-1.5	1155.9	0.29	6.93	3.80	0.78	H	RCB
V* V854 Cen	-10.9	231.3	-119.3	1462.0	0.43	11.53	4.61	3.18	TK	RCB
V* Z UMi	81.5	173.3	29.0	812.6	0.77	15.25	1.96	4.51	TK	RCB
V* S Aps	-117.0	242.1	85.0	1524.9	0.10	7.51	6.19	1.54	TK	RCB
V* R CrB	-50.3	241.7	34.9	1839.0	0.13	9.12	7.09	0.93	TH	RCB
V* IO Nor	-87.6	175.4	16.7	891.5	0.36	5.84	2.75	0.06	TK	RCB
V* RT Nor	-78.0	154.5	-6.6	808.1	0.23	4.70	2.92	0.76	TK	RCB
IRAS 16571-5011	-105.0	67.5	-117.3	452.3	0.48	5.15	1.79	2.84	H	RCB
V* GV Oph	49.2	150.2	-41.1	445.3	0.46	4.08	1.52	0.98	B	RCB
SV* HV 7863	-101.4	226.2	77.0	889.6	0.19	4.84	3.29	0.73	TK	RCB
ASAS J171710-2043.3	-139.2	65.4	-96.1	23.6	0.91	2.38	0.11	1.86	B	RCB
V* V2552 Oph	-21.0	122.1	-152.0	543.7	0.40	4.75	2.03	1.76	B	RCB
Terz V 2637	-112.4	37.0	60.5	-56.3	0.49	1.12	0.39	0.42	B	RCB
V* V653 Sco	-246.9	-40.6	99.1	233.1	0.92	13.08	0.51	2.55	H	RCB
V* WX CrA	35.0	88.6	-126.7	210.3	0.46	2.64	0.97	1.46	B	RCB
V* VZ Sgr	459.0	159.2	175.7	171.9	0.78	4.64	0.58	2.46	B	RCB
V* RS Tel	-35.3	72.5	9.7	194.7	0.60	3.60	0.91	1.41	B	RCB
V* FH Sct	14.9	267.1	-106.5	876.5	0.12	4.66	3.68	1.34	TK	RCB
V* V CrA	-5.1	338.5	30.3	3660.8	0.53	35.04	10.85	3.03	TK	RCB
V* SV Sge	25.6	239.9	34.1	1534.7	0.13	7.47	5.73	0.44	TH	RCB
V* V1157 Sgr	-1.7	260.5	34.3	1180.9	0.06	5.52	4.89	1.01	TH	RCB
V* RY Sgr	72.6	252.5	-55.1	1772.2	0.20	9.64	6.41	1.21	TK	RCB
V* ES Aql	-53.1	180.3	72.4	536.9	0.53	5.33	1.66	1.22	TK	RCB
V* V482 Cyg	-14.5	215.0	-18.3	1595.6	0.15	7.95	5.84	0.36	TH	RCB
V* UV Cas	52.4	220.3	4.5	2143.8	0.17	11.17	7.92	0.06	TH	RCB
IRAS 00450+7401	40.0	170.7	-18.4	3629.5	0.20	21.60	14.50	3.90	TK	RCB
V* W Men	-53.1	55.1	-142.1	425.4	0.62	9.60	2.25	7.98	H	RCB
HD 137613	-80.8	197.6	5.2	1351.8	0.30	8.09	4.37	0.63	TH	HdC
C* 2277	-185.7	91.5	50.0	536.6	0.38	4.14	1.87	0.90	H	HdC
SOPS IV e-67	-17.7	120.0	-123.5	638.4	0.44	6.25	2.43	3.20	H	HdC
V* LV TrA	-33.4	232.1	40.3	1504.5	0.09	7.01	5.89	0.61	TH	HdC
V* AC Ser	-46.8	156.2	19.1	-45.1	0.88	3.07	0.20	1.99	H	RCB
UCAC4 325-115052	-126.3	283.5	25.9	2899.1	0.50	25.39	8.46	1.10	TK	RCB
2MASS J17485129-3306172	108.8	336.9	38.3	3662.9	0.60	41.20	10.14	2.63	TK	RCB
2MASS J17510712-2423573	123.2	-89.0	54.8	-98.5	0.28	1.05	0.59	0.23	B	RCB
IRAS 18029-1513	-192.8	283.6	33.0	2015.0	0.56	18.85	5.37	0.79	H	RCB
ATO J277.4326-19.0462	-45.1	266.9	17.1	2507.8	0.21	14.00	9.15	0.39	TH	RCB
HD 173409	109.3	272.8	-55.3	4788.9	0.45	41.82	16.05	8.14	TK	HdC
V* V4152 Sgr	-52.4	172.9	-34.0	1024.8	0.32	6.48	3.31	0.81	TH	RCB
HD 182040	73.0	236.6	-7.8	1810.5	0.18	9.33	6.53	0.21	TH	HdC
CD-35 13668	54.1	360.8	9.2	4427.0	0.66	58.95	12.18	7.87	TK	HdC
C* 2891	37.0	247.9	-34.2	2386.5	0.07	13.13	11.35	5.35	TK	HdC
Ton S 137	-17.1	141.7	38.9	1100.9	0.44	8.28	3.23	1.06	TK	He-sdO
PG 0016+151	-31.8	239.8	-28.7	2113.6	0.12	10.91	8.61	2.21	TK	He-sdO
LAMOST J001954.03+510505.6	60.2	226.3	35.0	1899.2	0.26	10.95	6.50	0.80	TH	He-sdO
PB 6221	-87.2	122.3	-8.9	1271.5	0.51	13.30	4.36	6.67	H	He-sdO
LAMOST J010223.99+485245.3	-28.6	220.1	13.8	2768.5	0.17	15.14	10.78	1.62	TK	He-sdO
HS 0110+3222	-8.4	118.7	-57.3	1185.0	0.50	11.06	3.68	3.89	TK	He-sdO
PG 0113+259	59.3	231.1	-14.7	2015.9	0.20	10.89	7.33	0.90	TH	He-sdO
PB 6433	46.0	125.7	-15.2	1157.7	0.49	9.97	3.45	2.59	TK	He-sdO
GALEX J012630.2+503946	14.2	253.2	25.9	2804.5	0.17	15.26	10.93	1.42	TK	He-sdO
FBS 0132+370	18.5	265.3	-36.3	2442.2	0.18	13.32	9.28	1.44	TK	He-sdO
LAMOST J015012.51+254747.2	-99.9	66.7	76.5	631.0	0.77	12.05	1.59	4.23	H	He-sdO
Feige 19	42.5	253.3	10.1	2201.5	0.16	11.47	8.38	0.98	TH	He-sdO

Star	$U$ km s <sup>-1</sup>	$V$ km s <sup>-1</sup>	$W$ km s <sup>-1</sup>	$J_z$ kpc km s <sup>-1</sup>	$e$	$R_a$ kpc	$R_p$ kpc	$Z_{\max}$ kpc	pop	class
FBS 0212+385	31.4	262.3	-39.6	2192.0	0.16	11.50	8.27	0.91	TH	He-sdO
LAMOST J021703.37+544752.1	-51.1	195.3	17.6	2086.1	0.25	11.93	7.22	0.52	TH	He-sdO
LAMOST J023851.64+432309.5	-22.7	121.4	1.4	1146.3	0.54	10.11	3.02	0.55	TK	He-sdO
Feige 26	-26.6	216.3	99.0	2036.4	0.17	11.86	8.46	4.10	TK	He-sdO
PG 0310+149	37.6	246.0	8.4	2348.2	0.13	12.01	9.27	1.20	TH	He-sdO
UCAC4 551-007425	27.5	203.3	21.6	2040.6	0.11	10.02	8.11	1.07	TH	He-sdO
EC 03505-6929	-41.8	244.4	51.0	1921.5	0.14	9.99	7.47	1.65	TK	He-sdO
HE 0414-5429	-16.7	255.6	16.6	2148.8	0.13	11.09	8.50	1.69	TK	He-sdO
GALEX J041536.0+253857	-65.2	250.4	31.8	2524.7	0.24	14.87	9.06	1.29	TK	He-sdO
EC 04253-8213	-52.4	252.6	37.4	1878.7	0.18	10.19	7.07	1.76	TK	He-sdO
GALEX J042542.2-060934	-12.0	232.3	-8.0	2343.0	0.05	11.13	10.08	1.58	TK	He-sdO
BPS CS 22182-0037	1.8	288.5	39.1	2554.4	0.28	15.91	9.00	2.05	TK	He-sdO
UCAC4 434-007650	-55.1	277.4	47.8	2657.3	0.32	17.51	9.11	2.29	TK	He-sdO
GALEX J050231.9+091835	-11.0	199.7	-0.1	2182.0	0.15	11.26	8.34	0.91	TH	He-sdO
GALEX J050325.3+641909	-32.1	214.2	-7.3	2362.5	0.14	12.14	9.20	0.92	TH	He-sdO
GALEX J050650.6+193055	-44.5	198.0	20.2	1980.6	0.24	11.27	6.84	0.62	TH	He-sdO
GALEX J051157.7+235610	-6.3	172.0	38.5	2004.2	0.24	11.55	7.12	1.52	TK	He-sdO
UCAC4 535-014568	41.8	218.6	27.0	2194.4	0.05	10.18	9.17	0.74	TH	He-sdO
UCAC4 630-027754	18.8	191.9	13.8	1881.4	0.16	9.52	6.96	0.32	TH	He-sdO
KPD 0552+1903	-31.6	180.9	-15.1	1849.1	0.27	10.74	6.17	0.29	TH	He-sdO
LAMOST J055814.17+464025.3	13.9	231.4	2.0	2403.6	0.03	11.01	10.28	0.50	TH	He-sdO
UCAC4 498-020345	-110.5	264.8	27.7	2580.6	0.44	20.08	7.80	1.03	TK	He-sdO
LAMOST J060806.00+461001.4	19.8	190.8	2.5	2763.9	0.12	14.32	11.18	1.37	TK	He-sdO
GALEX J061205.9+473125	-1.0	165.8	30.7	2105.3	0.22	12.07	7.66	1.83	TK	He-sdO
LAMOST J061924.34+234639.8	-43.4	248.6	-22.6	2560.4	0.08	12.52	10.56	0.85	TH	He-sdO
UCAC4 555-028073	-1.6	243.0	18.7	2803.0	0.10	14.08	11.48	0.69	TH	He-sdO
LAMOST J062812.03+374234.5	-21.0	204.2	-11.7	2670.9	0.13	13.90	10.64	1.21	TK	He-sdO
KUV 06290+2813	25.1	201.1	41.7	2145.4	0.08	10.36	8.89	1.41	TK	He-sdO
UCAC4 566-028577	-33.2	139.4	-50.0	1339.2	0.45	10.31	3.94	1.65	TK	He-sdO
GALEX J063452.6+371110	37.5	151.9	6.2	2584.1	0.28	16.06	9.10	1.95	TK	He-sdO
TYC 1337-283-1	-61.4	253.2	3.3	2172.1	0.23	12.20	7.62	0.10	TH	He-sdO
FBS 0649+403	102.4	210.8	40.8	2116.4	0.28	12.89	7.25	1.47	TK	He-sdO
SDSS J065256.41+120300.8	-76.0	254.4	-49.7	3846.2	0.12	21.60	17.03	5.60	TK	He-sdO
HS 0657+5333	174.2	22.7	57.4	583.3	0.80	12.53	1.41	3.18	H	He-sdO
2MASS J07024049+1147418	-8.0	213.0	4.1	2309.7	0.09	11.18	9.28	0.44	TH	He-sdO
LAMOST J070801.51+103510.1	-4.9	247.2	3.9	2795.5	0.09	13.86	11.59	0.72	TH	He-sdO
GALEX J071503.2+750140	-119.6	-106.2	-21.6	-671.8	0.85	18.55	1.55	4.33	H	He-sdO
GALEX J072516.9+283831	8.6	263.1	18.9	2391.6	0.13	12.20	9.31	0.64	TH	He-sdO
LAMOST J072628.27+083747.9	-105.9	104.5	-72.4	1413.5	0.60	17.36	4.32	7.88	H	He-sdO
LAMOST J072835.11+280239.1	2.0	232.7	15.1	2604.5	0.04	12.24	11.39	1.34	TK	He-sdO
UCAC4 453-037143	-15.8	198.9	-28.7	2019.5	0.33	13.51	6.79	2.69	TK	He-sdO
LAMOST J073409.31+523028.6	-22.0	-92.3	-3.5	-278.4	0.91	12.27	0.58	1.56	H	He-sdO
HS 0735+4026	22.5	171.8	22.9	2192.6	0.17	11.93	8.53	2.24	TK	He-sdO
HS 0736+3953	38.6	123.5	32.0	2758.5	0.26	18.80	11.02	7.14	TK	He-sdO
FBS 0742+337	-54.6	275.9	-30.3	2641.5	0.11	13.74	11.03	2.48	TK	He-sdO
GALEX J075234.2+161604	-34.7	244.2	-2.7	2220.4	0.07	10.50	9.08	0.60	TH	He-sdO
GALEX J075250.0+305936	40.4	25.9	11.5	755.8	0.75	12.84	1.85	3.32	TK	He-sdO
BD+75 325	-22.6	243.7	0.8	2018.3	0.10	9.60	7.92	0.11	TH	He-sdO
GALEX J082751.0+410925	-17.7	322.1	12.8	1759.6	0.39	13.25	5.85	3.90	TK	He-sdO
[CW83] 0832 - 01	10.8	235.9	26.3	2109.4	0.11	10.35	8.29	0.68	TH	He-sdO
PG 0838+133	-69.2	253.4	-22.5	2230.2	0.19	12.10	8.28	1.13	TH	He-sdO
US 1993	4.1	58.9	9.3	609.0	0.76	10.65	1.46	1.97	TK	He-sdO
GALEX J090253.0+073533	25.4	-32.3	-17.4	306.3	0.91	16.08	0.75	6.47	H	He-sdO
[CW83] 0904 - 02	-84.0	315.3	-18.1	2189.9	0.17	11.69	8.26	1.24	TK	He-sdO
PG 0912+119	-71.9	118.9	-16.5	924.8	0.62	10.34	2.45	2.21	TK	He-sdO
PG 0914-037	-166.9	152.7	-71.1	971.9	0.47	9.93	3.55	5.26	H	He-sdO
Ton 414	-4.0	176.0	4.5	1850.6	0.25	10.77	6.40	1.26	TK	He-sdO
SBSS 0934+495	13.5	137.4	31.6	1715.3	0.33	12.29	6.17	4.39	TK	He-sdO
TYC 4895-599-1	-98.9	292.6	28.9	1856.0	0.35	12.25	5.93	1.37	TK	He-sdO
GD 300	-109.9	99.8	-0.1	-405.3	0.84	11.18	0.96	2.55	TK	He-sdO
GALEX J095601.7+091138	-54.8	217.1	-7.9	1887.0	0.17	10.00	7.06	1.33	TK	He-sdO
GALEX J095648.5+142241	-124.9	265.4	-48.6	1922.5	0.06	9.53	8.52	2.68	TK	He-sdO
Ton 1137	-73.5	204.0	-4.3	1463.8	0.36	10.25	4.84	2.65	TK	He-sdO
PG 1034+001	-51.8	277.8	59.9	1725.4	0.28	10.15	5.70	0.54	TH	He-sdO
GALEX J104033.8+562206	-7.5	188.4	33.6	1665.4	0.26	10.20	5.96	2.49	TK	He-sdO
PG 1038+510	-128.7	205.8	108.0	-250.5	0.95	21.02	0.50	3.76	TK	He-sdO

Star	$U$ km s <sup>-1</sup>	$V$ km s <sup>-1</sup>	$W$ km s <sup>-1</sup>	$J_z$ kpc km s <sup>-1</sup>	$e$	$R_a$ kpc	$R_p$ kpc	$Z_{\max}$ kpc	pop	class
GALEX J105759.3+470307	-1.0	215.2	16.4	2121.7	0.05	10.45	9.46	2.76	TK	He-sdO
SDSS J110215.45+024034.1	-138.1	100.0	-60.3	832.6	0.68	12.44	2.34	5.17	H	He-sdO
PG 1102+499	-53.9	210.7	-19.6	1627.2	0.23	9.37	5.91	1.96	TK	He-sdO
CBS 432	-95.0	193.2	29.6	1141.1	0.50	10.90	3.62	4.20	TK	He-sdO
PG 1125-055	-224.4	5.5	172.6	-782.5	0.61	10.10	2.48	4.83	H	He-sdO
PG 1134+463	-88.8	227.3	35.2	1216.1	0.46	9.79	3.59	1.97	TK	He-sdO
HS 1203+6650	-17.9	249.0	41.6	1496.1	0.45	11.99	4.57	2.95	TK	He-sdO
GALEX J123808.7+053318	-191.3	173.9	5.3	830.5	0.51	8.66	2.82	4.08	H	He-sdO
[BFS85] 12h30 2B1	-100.4	209.5	-4.7	1499.3	0.24	10.23	6.21	4.75	H	He-sdO
Ton 102	-11.2	208.5	93.8	1857.0	0.11	10.04	8.03	3.40	TK	He-sdO
Ton 109	-233.6	126.0	-94.8	240.0	0.56	9.33	2.63	8.93	H	He-sdO
PG 1249+762	-9.1	232.3	50.7	1541.8	0.37	10.58	4.86	1.75	TK	He-sdO
SDSS J125301.62+394622.2	-86.0	64.9	-111.5	905.1	0.71	14.29	2.39	5.30	H	He-sdO
PG 1251+019	-109.8	-11.9	-143.2	118.4	0.97	15.16	0.27	6.56	H	He-sdO
PB 4363	-306.5	207.1	81.0	837.0	0.46	10.95	4.04	8.13	H	He-sdO
Ton 143	-108.5	360.2	83.2	1658.6	0.55	17.39	5.00	6.37	H	He-sdO
PG 1316+212	-249.7	106.6	-18.8	-165.9	0.88	8.40	0.53	4.58	H	He-sdO
PG 1318+062	-110.3	304.4	86.9	1636.3	0.31	10.48	5.57	2.27	TK	He-sdO
PB 166	-36.8	267.3	-0.5	1694.9	0.25	9.75	5.81	1.07	TH	He-sdO
PG 1325+054	-48.9	310.7	37.5	1967.9	0.25	11.56	6.97	1.79	TK	He-sdO
GALEX J134738.3+043427	-165.8	181.7	29.6	767.8	0.40	8.00	3.44	5.26	H	He-sdO
CD-46 8926	-3.0	321.3	-45.4	2035.4	0.43	15.59	6.28	2.77	TK	He-sdO
SDSS J135707.35+010454.4	-279.3	115.0	49.2	81.3	0.90	7.67	0.41	5.74	H	He-sdO
PG 1401+289	-94.2	150.3	-64.2	875.9	0.50	8.52	2.81	3.32	TK	He-sdO
GALEX J140715.4+033147	-191.9	207.7	73.5	678.0	0.51	7.56	2.45	3.95	H	He-sdO
PG 1412+613	-20.8	202.4	-20.0	1692.1	0.17	8.97	6.42	1.61	TK	He-sdO
FBS 1412+004	-173.7	111.0	-12.9	377.6	0.69	7.61	1.39	4.87	H	He-sdO
PG 1427+196	-43.2	228.1	17.2	1609.9	0.11	7.97	6.37	1.36	TK	He-sdO
PG 1442+346	-23.0	173.7	-90.5	945.6	0.32	8.26	4.27	5.12	H	He-sdO
PG 1444+076	-414.9	31.7	80.7	-1228.6	0.32	7.83	4.08	1.50	H	He-sdO
GALEX J144738.3+615033	-10.1	232.4	77.2	1724.5	0.22	11.22	7.11	4.82	TK	He-sdO
GALEX J145134.2+252221	18.3	207.9	-91.2	1389.4	0.19	8.58	5.87	3.67	TK	He-sdO
PG 1502+129	-8.5	270.8	22.6	1284.1	0.38	9.71	4.37	3.31	TK	He-sdO
PG 1507-015	-63.9	259.7	62.1	1401.8	0.12	7.28	5.72	1.96	TK	He-sdO
GALEX J151415.6-012925	-164.2	180.1	56.2	587.4	0.60	6.79	1.72	1.83	TK	He-sdO
PG 1528+029	-87.7	229.7	56.9	1141.2	0.26	6.96	4.08	1.75	TK	He-sdO
PG 1534-018	66.6	252.0	-53.4	1957.4	0.26	11.91	6.92	2.28	TK	He-sdO
PG 1539+442	-118.9	218.6	72.4	1315.3	0.24	9.33	5.69	4.84	H	He-sdO
PG 1539+043	-180.0	254.6	137.5	-92.0	0.81	6.65	0.69	6.01	H	He-sdO
SDSS J154801.15-023452.3	-130.2	130.0	16.7	-256.4	0.47	6.30	2.27	5.79	H	He-sdO
PG 1554+222	-11.1	221.5	13.9	1288.8	0.32	8.10	4.21	1.25	TK	He-sdO
PG 1555+504	28.5	254.5	99.6	1344.0	0.49	11.86	4.11	3.50	TK	He-sdO
PG 1555+489	-54.1	222.6	76.6	1202.2	0.34	8.63	4.25	3.03	TK	He-sdO
GALEX J160053.0-044132	-98.6	195.8	44.1	874.7	0.47	7.11	2.53	0.95	TK	He-sdO
GALEX J160152.8-040949	84.3	133.8	-205.8	1089.9	0.53	12.63	3.85	7.02	H	He-sdO
PG 1607+228	-37.3	224.1	25.7	1299.7	0.13	7.08	5.41	2.26	TK	He-sdO
PG 1610+043	-65.6	227.4	44.9	1157.1	0.19	6.53	4.40	1.70	TK	He-sdO
PG 1611+041	-136.3	176.0	24.4	792.2	0.47	6.88	2.46	1.84	TK	He-sdO
GALEX J161627.1-002933	-81.1	217.9	32.2	1101.4	0.20	6.38	4.22	1.84	TK	He-sdO
Ton 257	-182.5	172.3	97.8	113.4	0.92	7.20	0.31	3.35	H	He-sdO
GALEX J162411.5+312252	74.4	166.3	80.7	-234.8	0.87	11.16	0.81	8.21	H	He-sdO
PG 1624+382	-27.9	241.8	53.5	1561.5	0.12	7.99	6.24	1.78	TK	He-sdO
GALEX J162626.2+333314	19.7	231.4	81.6	920.2	0.51	9.13	2.96	3.70	TK	He-sdO
PG 1624+085	-37.5	198.8	-2.4	1224.5	0.27	7.22	4.11	0.96	TH	He-sdO
PG 1625-034	42.3	232.6	6.3	1342.2	0.32	8.37	4.35	1.09	TH	He-sdO
GALEX J170045.5+604307	49.1	246.5	82.8	2065.0	0.30	15.11	8.10	6.62	TK	He-sdO
PG 1700+198	-88.5	240.3	103.5	1124.4	0.26	7.13	4.15	2.27	TK	He-sdO
PG 1703+355	2.5	241.8	89.4	1356.4	0.32	8.92	4.63	2.26	TK	He-sdO
GALEX J171720.5+094131	-37.6	126.5	-43.5	576.8	0.57	6.33	1.73	1.70	TK	He-sdO
GALEX J174516.3+244348	-76.3	120.9	-109.2	717.6	0.53	8.10	2.49	4.01	H	He-sdO
GALEX J175548.5+501210	63.6	200.6	8.0	1549.3	0.30	9.29	4.96	0.33	TH	He-sdO
LAMOST J181712.86+053202.7	-41.7	205.8	12.5	1010.3	0.27	5.92	3.39	0.61	TH	He-sdO
GALEX J182208.6+103745	72.0	281.3	17.8	1217.4	0.18	6.79	4.71	1.85	TK	He-sdO
UCAC4 687-068720	14.2	277.3	9.7	2210.4	0.19	11.90	8.16	0.82	TH	He-sdO
LAMOST J193312.83+380154.6	-48.6	237.2	21.4	1670.1	0.16	8.54	6.17	0.80	TH	He-sdO
BPS CS 22896-0128	43.1	213.0	42.1	1115.5	0.12	6.01	4.69	1.98	TK	He-sdO



Star	$U$ km s <sup>-1</sup>	$V$ km s <sup>-1</sup>	$W$ km s <sup>-1</sup>	$J_z$ kpc km s <sup>-1</sup>	$e$	$R_a$ kpc	$R_p$ kpc	$Z_{\max}$ kpc	pop	class
LAMOST J202546.17+092158.7	-29.2	221.5	56.6	1173.3	0.23	6.97	4.34	1.88	TK	He-sdO
LAMOST J202610.56+055413.9	22.0	194.3	-8.6	1361.8	0.21	7.28	4.77	0.65	TH	He-sdO
LAMOST J210936.02+362337.5	-41.3	227.9	4.5	1892.2	0.15	9.56	7.08	0.56	TH	He-sdO
HS 2108+1413	-39.0	273.8	-15.9	2108.2	0.20	11.41	7.64	0.66	TH	He-sdO
PG 2110+001	-103.0	206.2	25.2	1298.7	0.34	8.62	4.24	1.73	TK	He-sdO
LAMOST J211624.57+132338.7	99.8	19.5	28.2	209.4	0.88	11.70	0.73	8.23	H	He-sdO
GALEX J211832.4+233416	-48.1	218.1	9.3	1652.4	0.18	8.60	5.95	0.63	TH	He-sdO
PG 2116+008	35.9	224.3	-8.2	1568.9	0.11	7.86	6.25	1.54	TK	He-sdO
GALEX J211925.9+202155	24.5	128.7	-73.7	1014.1	0.42	8.00	3.28	2.40	TK	He-sdO
GALEX J212356.6+153323	63.0	90.5	-42.9	718.7	0.61	8.05	1.94	1.56	TK	He-sdO
GALEX J212504.4+212957	13.8	244.6	21.9	1868.4	0.05	8.78	8.00	1.66	TK	He-sdO
GALEX J212544.4+202812	-61.1	237.9	9.7	1844.4	0.18	9.64	6.64	0.38	TH	He-sdO
UCAC4 648-107111	-22.2	254.9	-5.9	2089.3	0.12	10.26	8.07	0.24	TH	He-sdO
GALEX J214106.6+252832	-92.7	239.8	0.3	1886.5	0.29	11.25	6.23	0.47	TH	He-sdO
SDSS J214226.13+091307.5	140.4	50.0	53.4	408.0	0.78	9.03	1.09	3.73	H	He-sdO
GALEX J214540.8-012807	2.1	83.9	7.4	589.6	0.65	7.54	1.59	1.46	TK	He-sdO
UCAC4 637-113968	4.7	314.8	-50.9	2573.2	0.37	18.22	8.31	1.89	TK	He-sdO
PHL 149	-72.0	179.7	32.1	1282.8	0.35	8.39	4.08	1.23	TK	He-sdO
PG 2158+082	-196.5	260.6	-72.6	1998.7	0.58	20.97	5.55	4.84	H	He-sdO
PG 2201+145	-7.2	227.7	-34.7	1786.7	0.04	8.14	7.58	1.18	TH	He-sdO
SDSS J220819.50+060255.4	-73.3	183.2	26.8	1310.5	0.33	9.48	4.73	3.58	TK	He-sdO
BPS CS 22956-0090	16.3	120.0	69.5	817.5	0.52	7.68	2.45	2.09	TK	He-sdO
BPS CS 22892-0051	151.3	134.4	94.6	1000.4	0.51	10.38	3.39	4.99	H	He-sdO
BPS CS 22881-0069	48.7	256.4	26.5	1927.0	0.18	10.33	7.11	1.21	TK	He-sdO
GALEX J223455.5+312325	56.9	182.7	63.9	1592.0	0.23	9.49	5.93	2.60	TK	He-sdO
PHL 364	-7.8	167.8	-49.2	1291.0	0.28	8.05	4.54	2.03	TK	He-sdO
PG 2244+153	130.3	120.4	26.9	963.2	0.60	10.14	2.54	1.82	TK	He-sdO
PG 2249+220	11.7	188.0	11.7	1605.4	0.20	8.90	5.93	1.76	TK	He-sdO
BPS CS 22938-0044	20.3	230.2	52.2	1531.2	0.15	8.26	6.12	2.28	TK	He-sdO
GALEX J230124.7+325943	50.9	87.8	37.9	831.7	0.66	11.02	2.27	3.69	TK	He-sdO
FBS 2307+338	10.8	213.8	30.8	1864.7	0.08	8.88	7.56	1.11	TH	He-sdO
BPS CS 22938-0073	-33.5	128.8	17.8	865.0	0.53	7.73	2.41	1.07	TK	He-sdO
PG 2333-002	76.1	137.3	74.5	1114.1	0.35	9.40	4.53	5.04	H	He-sdO
GALEX J233913.9+134215	117.1	113.0	-84.8	960.5	0.63	12.31	2.76	4.83	TK	He-sdO
PG 2343+267	26.2	224.4	13.7	2145.5	0.06	10.48	9.31	2.30	TK	He-sdO
GALEX J235050.1+194628	56.8	205.0	47.6	2056.4	0.13	11.87	9.22	4.85	TK	He-sdO
PG 2352+181	105.6	190.9	-22.2	1548.4	0.40	10.84	4.63	0.80	TK	He-sdO
GALEX J014640.5+411826	23.8	264.3	9.3	2746.5	0.19	15.39	10.44	1.51	TK	He-sdB
UCAC4 450-010156	8.1	243.1	5.8	2219.6	0.05	10.18	9.26	0.38	TH	He-sdB
GALEX J062038.5-570538	-16.2	272.9	5.9	2229.0	0.16	11.56	8.44	0.64	TH	He-sdB
GALEX J064024.8+444720	-3.1	249.6	13.4	2474.0	0.10	12.26	9.99	0.75	TH	He-sdB
GALEX J064918.3+235440	34.5	226.9	25.5	2495.9	0.07	11.96	10.47	0.97	TH	He-sdB
FBS 0654+366	-3.5	286.1	-4.2	2391.1	0.19	12.92	8.85	0.45	TH	He-sdB
HZ 38	-83.2	264.7	-21.6	1538.0	0.25	9.05	5.44	1.80	TK	He-sdB
GALEX J145817.5+022807	-36.9	240.8	16.9	874.4	0.11	7.86	6.32	6.29	H	He-sdB
PG 1607+174	-39.0	228.0	12.4	1684.5	0.12	8.13	6.41	0.48	TH	He-sdB
FBS 1749+373	21.4	193.2	4.7	1416.2	0.28	8.25	4.61	0.40	TH	He-sdB
UCAC4 657-066324	3.4	232.4	3.8	1791.1	0.04	7.99	7.37	0.46	TH	He-sdB
2MASS J19230068+3715044	-68.6	247.0	-32.9	1832.1	0.22	10.12	6.49	0.98	TH	He-sdB
GALEX J213308.4+064701	-76.8	287.1	52.6	2991.3	0.39	23.22	10.31	6.43	TK	He-sdB
UCAC4 653-107038	-29.6	212.6	-5.9	1817.2	0.15	9.14	6.74	0.46	TH	He-sdB
2MASS J21391157+4539155	-72.3	182.6	-17.8	1815.0	0.32	11.38	5.82	0.70	TH	He-sdB
JL 87	-24.2	264.9	8.7	2043.0	0.15	10.45	7.67	0.59	TH	He-sdB
BPS CS 22956-0094	63.8	184.2	21.7	1232.8	0.48	9.66	3.41	0.51	TH	He-sdB
UCAC4 685-001272	-4.8	231.1	26.0	2073.9	0.05	9.48	8.64	0.64	TH	He-sdOB
GALEX J001306.4+491149	114.6	58.2	29.8	-20.8	0.98	12.99	0.11	1.44	H	He-sdOB
GALEX J002433.0+264910	-4.2	226.2	16.2	2145.4	0.04	10.12	9.34	1.82	TK	He-sdOB
FBS 0035+343	35.7	302.5	-41.4	2604.3	0.35	17.68	8.61	1.67	TK	He-sdOB
PG 0039+135	-22.8	191.0	72.8	1607.6	0.19	8.96	6.08	2.10	TK	He-sdOB
PB 6244	188.0	102.9	55.4	994.0	0.63	15.49	3.53	9.76	H	He-sdOB
PB 6275	163.0	-22.4	-116.1	-219.4	0.92	13.70	0.58	7.41	H	He-sdOB
GALEX J011928.8+490109	13.1	239.5	-9.6	2048.5	0.05	9.28	8.46	0.25	TH	He-sdOB
GALEX J014326.2+323439	-11.7	50.0	68.6	385.4	0.82	9.94	0.95	3.72	TK	He-sdOB
PG 0216+246	-38.3	250.8	8.7	2480.3	0.16	13.40	9.64	1.79	TK	He-sdOB
GALEX J022125.9+085919	-86.3	161.6	-14.2	1884.2	0.37	14.76	6.76	5.92	TK	He-sdOB

Star	$U$ km s <sup>-1</sup>	$V$ km s <sup>-1</sup>	$W$ km s <sup>-1</sup>	$J_z$ kpc km s <sup>-1</sup>	$e$	$R_a$ kpc	$R_p$ kpc	$Z_{\max}$ kpc	pop	class
PG 0221+217	-122.6	151.6	-16.9	1336.9	0.52	11.52	3.65	1.26	TK	He-sdOB
GALEX J022422.2+000313	21.2	-33.8	-39.2	-297.3	0.89	12.93	0.78	6.54	H	He-sdOB
GALEX J023254.0+370419	-75.1	218.0	1.1	1949.4	0.26	11.23	6.62	0.45	TH	He-sdOB
PG 0240+046	32.6	164.2	93.0	1482.0	0.20	8.84	5.87	3.04	TK	He-sdOB
KUV 02445+3633	21.1	295.9	-90.1	2562.5	0.35	18.10	8.79	4.03	TK	He-sdOB
GALEX J031842.4+340554	-19.9	202.6	9.7	1875.7	0.17	9.65	6.87	0.45	TH	He-sdOB
KPD 0319+4553	78.9	255.8	-12.8	2293.9	0.27	13.59	7.87	0.33	TH	He-sdOB
HD 275347	-35.6	230.9	2.8	1998.0	0.12	9.77	7.65	0.13	TH	He-sdOB
BPS CS 22190-0003	-73.8	277.7	-6.5	2399.4	0.26	14.49	8.42	1.49	TK	He-sdOB
HZ 3	-18.8	232.2	35.4	2006.8	0.10	9.65	7.97	0.74	TH	He-sdOB
GALEX J041700.7+350717	34.4	239.0	12.2	2356.8	0.10	11.51	9.44	0.45	TH	He-sdOB
UCAC4 633-017614	31.3	167.9	17.5	1578.5	0.28	9.14	5.18	0.39	TH	He-sdOB
KUV 04456+1502	22.4	203.2	16.9	1990.2	0.10	9.58	7.83	0.60	TH	He-sdOB
GALEX J045027.6+155910	32.5	218.7	5.1	2216.0	0.07	10.45	9.08	0.59	TH	He-sdOB
GALEX J052300.5+182727	43.7	196.7	14.0	2004.2	0.13	10.00	7.62	0.46	TH	He-sdOB
SDSS J052933.85+040720.0	-98.9	186.6	-11.1	1837.3	0.39	12.77	5.57	0.74	TK	He-sdOB
GALEX J053656.5+395516	15.6	203.5	12.9	1868.9	0.12	9.05	7.14	0.26	TH	He-sdOB
LAMOST J054711.59+170919.5	7.3	213.9	12.9	2074.6	0.07	9.67	8.37	0.29	TH	He-sdOB
ATO J089.4285+27.7808	215.1	196.7	14.9	2195.6	0.61	23.07	5.66	0.71	H	He-sdOB
LAMOST J060000.23+112836.6	-56.1	213.6	-28.0	2030.4	0.19	10.85	7.42	0.81	TH	He-sdOB
EC 05593-5901	-39.2	249.0	57.7	2148.3	0.25	12.93	7.80	2.60	TK	He-sdOB
Lan 11	-80.0	248.8	-6.5	2211.4	0.25	12.72	7.66	0.20	TH	He-sdOB
LAMOST J062830.43+112018.4	4.8	237.8	8.4	2313.4	0.02	10.38	9.91	0.13	TH	He-sdOB
LAMOST J062836.51+325031.5	-11.9	198.0	-17.1	1855.7	0.18	9.70	6.70	0.44	TH	He-sdOB
LAMOST J063650.09+291925.0	26.0	225.9	13.2	2745.2	0.06	13.23	11.68	0.90	TH	He-sdOB
LAMOST J064701.65+690625.2	58.5	187.0	5.6	2113.6	0.24	12.39	7.53	1.76	TK	He-sdOB
LAMOST J070828.40+442534.8	-1.1	144.2	-40.8	1283.4	0.44	9.75	3.80	1.52	TK	He-sdOB
GALEX J071319.6+380740	88.5	84.4	3.4	960.6	0.65	10.98	2.35	0.88	TK	He-sdOB
GALEX J071401.4+693321	-14.8	-70.7	-96.1	-742.3	0.63	10.64	2.44	5.73	H	He-sdOB
[CW83] 0711 + 22	-41.8	246.9	-11.5	2036.6	0.10	9.77	7.98	0.28	TH	He-sdOB
GALEX J071856.2+102637	-17.0	227.1	6.3	2098.4	0.09	9.96	8.36	0.28	TH	He-sdOB
GALEX J072315.6+183457	26.2	208.3	6.7	2150.4	0.19	11.66	7.86	0.82	TH	He-sdOB
GALEX J072824.7+414953	-31.5	205.0	-11.2	2159.8	0.17	11.50	8.11	1.15	TH	He-sdOB
GALEX J073220.1+270408	77.1	189.6	18.6	1773.4	0.40	12.49	5.34	0.91	TH	He-sdOB
GALEX J074125.1+125020	-23.8	217.2	16.9	2601.7	0.17	14.14	10.12	1.78	TK	He-sdOB
LAMOST J075139.26+064604.8	-41.0	225.9	-11.2	1937.3	0.13	9.52	7.38	0.37	TH	He-sdOB
SDSS J075733.11+235828.1	29.1	166.9	42.9	2230.8	0.21	13.24	8.71	3.69	TK	He-sdOB
GALEX J075807.5-043203	-94.0	293.7	-16.8	2558.3	0.45	20.06	7.65	0.51	TK	He-sdOB
KUV 07564+3723	-16.1	226.7	-3.6	2163.1	0.06	10.12	9.05	1.00	TH	He-sdOB
[CW83] 0825 + 15	-55.4	283.5	-17.9	2178.0	0.12	10.87	8.46	0.61	TH	He-sdOB
Ton 927	-6.5	163.2	3.5	1611.4	0.29	9.60	5.23	0.52	TH	He-sdOB
Ton 380	-23.7	223.8	-0.9	2056.3	0.11	10.13	8.11	0.95	TH	He-sdOB
PG 0902+057	-48.6	241.3	4.6	1732.0	0.21	9.30	6.12	0.63	TH	He-sdOB
GALEX J094044.0+004759	-122.9	259.4	-22.6	2118.2	0.07	10.42	9.08	2.25	TK	He-sdOB
PG 0950+158	-105.3	138.6	-67.6	1187.3	0.52	11.07	3.45	3.10	TK	He-sdOB
Ton 554	-52.9	-3.7	-108.7	695.3	0.85	19.28	1.57	4.23	H	He-sdOB
PG 1127+019	-85.3	245.1	-26.9	1730.7	0.11	8.52	6.89	1.37	TK	He-sdOB
Feige 46	-208.3	219.7	77.2	470.3	0.80	9.58	1.07	0.56	H	He-sdOB
Feige 49	-171.6	208.7	58.6	870.6	0.58	8.62	2.26	0.71	H	He-sdOB
GALEX J120521.5+224702	-193.3	264.9	161.0	1157.7	0.64	16.48	3.66	8.77	H	He-sdOB
CBS 461	-180.5	262.7	83.2	437.7	0.85	12.71	1.02	4.47	H	He-sdOB
CBS 58	-95.0	192.3	180.8	1032.9	0.32	9.70	5.01	6.60	H	He-sdOB
GALEX J124552.8+175111	-224.3	188.3	140.5	410.8	0.78	9.11	1.11	3.85	H	He-sdOB
PG 1258+012	-117.2	310.0	76.1	1762.7	0.28	11.08	6.30	2.55	TK	He-sdOB
PB 146	-64.2	139.9	-17.7	1309.1	0.45	10.28	3.93	2.13	TK	He-sdOB
Cl* NGC 5139 LEID 49021	-179.6	27.8	35.1	91.5	0.93	9.15	0.32	0.87	H	He-sdOB
2QZ J132542.4-014655	-90.3	223.9	10.5	1406.0	0.15	7.81	5.72	2.46	TK	He-sdOB
Cl* NGC 5139 LEID 40026	-174.1	42.6	60.8	262.9	0.90	10.46	0.58	1.57	H	He-sdOB
Cl* NGC 5139 LEID 31031	-86.5	-227.3	-181.5	-819.1	0.13	9.97	7.65	8.87	H	He-sdOB
NGC 5139 5596	-156.4	68.9	53.3	457.9	0.81	9.75	1.04	1.23	H	He-sdOB
Cl* NGC 5139 LEID 42032	-143.2	86.8	87.7	762.1	0.71	11.76	1.97	3.83	H	He-sdOB
2MASS J13260202-4737234	-102.4	-203.4	-152.5	-518.2	0.14	8.35	6.29	7.81	H	He-sdOB
NGC 5139 4465	-175.6	36.7	52.3	197.4	0.92	9.95	0.44	1.21	H	He-sdOB
NGC 5139 6139	-194.9	-61.8	-41.7	-385.2	0.73	7.21	1.11	2.75	H	He-sdOB
Cl* NGC 5139 LEID 56042	-100.3	121.3	119.9	1447.2	0.52	15.37	4.89	7.57	H	He-sdOB
Cl* NGC 5139 LEID 54050	-119.1	109.0	115.5	1177.5	0.58	14.10	3.75	6.85	H	He-sdOB

Star	$U$ km s <sup>-1</sup>	$V$ km s <sup>-1</sup>	$W$ km s <sup>-1</sup>	$J_z$ kpc km s <sup>-1</sup>	$e$	$R_a$ kpc	$R_p$ kpc	$Z_{\max}$ kpc	pop	class
CI* NGC 5139 LEID 48062	-180.7	41.1	62.9	195.7	0.92	9.93	0.42	1.46	H	He-sdOB
CI* NGC 5139 LEID 58063	-128.0	94.1	83.1	921.4	0.65	12.15	2.54	3.70	H	He-sdOB
CI* NGC 5139 LEID 49227	-131.6	99.4	81.2	862.3	0.66	11.21	2.26	3.04	H	He-sdOB
CI* NGC 5139 LEID 56098	-184.5	30.8	56.7	113.2	0.95	9.69	0.24	1.24	H	He-sdOB
NGC 5139 4547	-117.5	112.5	81.3	1034.6	0.60	11.42	2.87	3.21	TK	He-sdOB
CI* NGC 5139 LEID 34202	-161.3	66.1	55.4	428.5	0.82	9.90	0.99	1.27	H	He-sdOB
CI* NGC 5139 LEID 56132	-131.6	92.2	92.8	958.5	0.67	13.13	2.63	4.82	H	He-sdOB
CI* NGC 5139 LEID 56141	-105.5	104.7	95.4	1438.7	0.59	16.42	4.27	6.41	TK	He-sdOB
CI* NGC 5139 LEID 50311	-156.4	72.2	66.5	526.1	0.79	10.47	1.23	1.89	H	He-sdOB
CI* NGC 5139 LEID 37330	-199.1	-12.2	16.4	-213.4	0.88	8.23	0.54	0.72	H	He-sdOB
NGC 5139 3595	-186.5	-17.4	-17.2	-202.1	0.89	8.07	0.46	1.00	H	He-sdOB
NGC 5139 4373	-190.3	3.3	11.8	-97.6	0.92	8.23	0.34	0.80	H	He-sdOB
SDSS J133449.25+041014.8	-185.8	132.8	-2.9	479.7	0.68	7.95	1.49	3.76	H	He-sdOB
GALEX J134352.1+394008	-213.6	174.0	130.1	139.5	0.89	9.25	0.51	6.75	H	He-sdOB
UM 610	-127.5	139.2	-35.1	757.4	0.55	8.11	2.37	3.18	TK	He-sdOB
GALEX J134621.2+224835	-141.3	249.9	102.2	971.1	0.47	9.21	3.32	4.16	H	He-sdOB
GALEX J135150.6+035718	-248.1	91.4	31.3	243.1	0.75	9.26	1.32	7.91	H	He-sdOB
PB 1353	-110.2	170.9	61.6	1080.5	0.37	9.53	4.43	5.42	H	He-sdOB
PG 1413+114	-98.9	236.0	50.8	1182.0	0.25	7.65	4.54	2.85	TK	He-sdOB
GALEX J143729.2-021507	-59.4	271.8	41.5	1523.9	0.22	8.53	5.45	1.43	TK	He-sdOB
GALEX J145522.9+045802	-62.0	209.6	1.7	1249.4	0.22	7.25	4.62	1.84	TK	He-sdOB
GALEX J145614.5+165740	-274.3	147.9	104.2	-63.9	0.96	7.47	0.17	3.75	H	He-sdOB
GALEX J152208.0+342503	-124.7	172.4	12.2	1210.7	0.41	10.77	4.53	5.46	H	He-sdOB
CSO 1099	-53.9	244.8	73.3	1343.7	0.24	8.16	4.95	2.36	TK	He-sdOB
SDSS J153419.42+372557.2	-71.7	229.1	64.4	1373.9	0.22	7.97	5.09	2.03	TK	He-sdOB
GALEX J155202.7+261542	-51.7	189.7	0.2	1035.3	0.37	7.43	3.44	2.02	TK	He-sdOB
PG 1559+048	-22.5	242.4	28.2	1602.8	0.16	8.13	5.84	0.54	TH	He-sdOB
PG 1614+270	-107.4	231.1	41.7	1609.4	0.30	10.32	5.59	2.55	TK	He-sdOB
GALEX J162051.0+375059	-42.5	233.6	47.7	1452.2	0.13	7.79	6.05	2.41	TK	He-sdOB
GALEX J163150.9+480431	82.8	107.3	-100.3	718.1	0.45	9.15	3.44	6.69	H	He-sdOB
SDSS J164042.90+311734.6	-207.6	239.6	220.8	524.0	0.38	7.92	3.54	6.76	H	He-sdOB
Ton 261	66.4	203.0	-50.6	1540.7	0.14	8.05	6.11	1.90	TK	He-sdOB
PG 1652+159	-21.5	215.9	21.1	1284.1	0.22	7.13	4.55	1.11	TH	He-sdOB
GALEX J170045.1+391830	-131.8	308.8	92.1	1578.8	0.21	11.79	7.71	7.19	H	He-sdOB
PG 1715+273	-27.8	228.9	16.0	1465.2	0.10	7.23	5.90	1.46	TK	He-sdOB
UCAC4 530-064631	-42.1	257.1	24.9	1685.3	0.12	8.42	6.57	1.28	TK	He-sdOB
GALEX J172034.1+145940	-246.4	11.3	-33.1	-557.2	0.72	8.61	1.43	1.78	H	He-sdOB
GALEX J172533.3+523321	-45.1	187.1	-3.9	1366.9	0.30	8.47	4.54	1.39	TK	He-sdOB
GALEX J181102.8+173759	255.4	-21.6	-60.2	-219.9	0.91	13.69	0.68	5.02	H	He-sdOB
HS 1837+5913	-46.8	277.4	-7.2	2287.4	0.26	13.54	7.93	0.84	TH	He-sdOB
2MASS J19271504+3827186	-27.9	236.6	-28.7	1811.7	0.10	8.68	7.10	0.71	TH	He-sdOB
2MASS J19380163+4649446	0.0	331.0	56.6	4101.1	0.37	31.64	14.59	7.55	TK	He-sdOB
2MASS J19565555+4350171	-8.7	271.2	-17.2	2195.7	0.17	11.51	8.15	0.35	TH	He-sdOB
BPS CS 22940-0009	1.2	138.3	-20.9	873.5	0.43	6.79	2.70	1.38	TK	He-sdOB
GALEX J211000.6+152913	-13.3	165.6	17.9	1194.3	0.35	7.71	3.75	0.84	TH	He-sdOB
GALEX J211148.7+132529	66.1	-96.7	-145.9	-526.0	0.56	8.35	2.35	5.95	H	He-sdOB
SDSS J212330.46+004238.8	33.4	196.4	50.5	1359.7	0.18	7.54	5.19	1.90	TK	He-sdOB
GALEX J213054.5-004116	-18.6	210.9	-0.3	1409.2	0.13	7.35	5.69	1.92	TK	He-sdOB
PG 2129+151	62.9	224.1	-70.2	1803.0	0.17	9.70	6.83	1.75	TK	He-sdOB
GALEX J215541.6+300340	-15.2	192.8	21.3	1559.0	0.21	8.40	5.47	0.71	TH	He-sdOB
GALEX J215956.5+141804	-42.2	260.4	23.2	2014.9	0.17	10.61	7.54	1.11	TH	He-sdOB
PG 2204+071	8.3	238.0	-26.5	1858.5	0.03	8.38	7.90	1.03	TH	He-sdOB
PG 2218+052	40.2	201.0	-52.5	1601.4	0.18	8.51	5.93	1.34	TK	He-sdOB
FBS 2255+404	-44.0	193.7	15.5	1797.8	0.24	10.10	6.24	0.85	TH	He-sdOB
PG 2321+214	70.9	233.7	-67.9	1901.5	0.25	11.29	6.78	2.08	TK	He-sdOB
LAMOST J232812.94+295333.5	-127.0	-26.9	55.3	-329.2	0.86	12.19	0.95	4.27	H	He-sdOB
GALEX J232856.6+492806	-25.0	194.3	-32.4	2138.2	0.16	11.28	8.17	1.41	TK	He-sdOB
Ton S 103	65.5	193.9	164.4	1475.3	0.18	10.67	7.45	6.56	H	He-sdOB